University of Nevada, Reno

# Geologic mapping and zircon (U-Th)/He thermochronology of the Avawatz Mountains, California; Implications for the eastern terminus of the Garlock fault

A thesis submitted in partial fulfillment of the requirements
for the degree of Master of Science in Geology

by

Wes M. Johns

Dr Andrew V. Zuza – Thesis Advisor

August, 2023

THE GRADUATE SCHOOL

We recommend that the thesis
prepared under our supervision by

entitled

be accepted in partial fulfillment of the
requirements for the degree of

*Advisor*

*Committee Member*

*Graduate School Representative*

Markus Kemmelmeier, Ph.D., Dean
*Graduate School*

## ABSTRACT

The Avawatz Mountains are located at the eastern tip of the left-slip Garlock fault where the fault intersects the NW-striking right-slip Southern Death Valley fault (SDVF). The Avawatz Mountains were constructed via late Cenozoic contractional deformation involving active thrust and/or oblique-slip faults. Contrasting structural models suggest that the Avawatz Mountains formed as either a fault-termination thrust belt at the eastern end of the Garlock fault, or within a transpressional restraining bend along the SDVF.

Here we present detailed geologic mapping, structural analysis, and low-temperature thermochronology data to test these proposed structural and evolutionary models and to resolve the timing and kinematics of deformation. Field observations show numerous subvertical west-striking strike-slip faults in the western portion of the range and a prominent west-dipping reverse fault along the eastern rangefront. Zircon (U-Th)/He thermochronology (ZHe) from a ~1 km vertical transect in the hanging wall of the eastern rangefront fault yields cooling ages ranging from 79 ± 11 Ma in the structurally highest samples to 12.3 ± 3.1 Ma in the structurally lowest samples. Across the vertical sampling transect, most samples yield average cooling ages that cluster around ca. 15 Ma. This age distribution is consistent with exhumation initiating in the middle Miocene (ca. 20-15 Ma), synchronous with the initiation of slip on the Garlock fault. Vertical exhumation rates calculated from ZHe data are < 1 mm/yr, which corresponds to a horizontal shortening rate of ~1 mm/yr based on the observed dip of the primary west-dipping reverse fault structure. Our observations suggest a complex

fault and exhumation history that may reflect the transfer of left-lateral slip on the Garlock fault to an east-directed termination thrust system that was later overprinted by slip on the SDVF and the development of a restraining bend.

## ACKNOWLEDGMENTS

First, I would like to thank my advisor Andrew Zuza for giving me this opportunity and providing me with the tools and knowledge to complete this project. Thank you to my committee members, Mike Darin and Scott Bassett for your valuable feedback and constant encouragement throughout this process. Thanks to Jim Metcalf at the CuTRaIL lab at the University of Colorado, Boulder for the (U-Th)/He thermochronology analyses. Thanks to Margo Odlum at the Nevada Plasma Facility Lab at the University of Nevada, Las Vegas for the U-Pb analyses. Thanks to my fellow graduate student Dominik Vlaha for accompanying me on mapping expeditions, as well as the countless conversations in the office and the field. I would like to thank the faculty and my fellow graduate students at University of Nevada, Reno who I have crossed paths with these last two years. I was extremely lucky to have you share your knowledge and build memories in class and in the field. Finally, I would like to thank my family and loved ones for encouraging and supporting me, without you none of this would have been possible. Support for this work was provided by USGS EdMap (Grant No. GS22AS00060). Additional funding was provided by a Geological Society of America Graduate Student Research Grant.

## TABLE OF CONTENTS

# LIST OF TABLES

## LIST OF FIGURES

## INTRODUCTION

In western North America, ~50 mm/yr of relative plate motion is accommodated between the Pacific and North American plates (Thatcher et al., 2016), with right-lateral shear distributed between the San Andreas fault (SAF) and the Eastern California Shear Zone (ECSZ). Although the primary Pacific-North American plate boundary trends NNW, there are numerous ENE-striking subparallel strike-slip faults oriented oblique to the regional shear zone trend (Schermer et al., 1996; McGill et al., 2009; Platt and Becker, 2013) (Fig. 1). The largest of 0these is the ~260 km-long, NE-striking, left-slip Garlock fault (Hess, 1910; Hill and Dibblee, 1953; Smith, 1962; Michael, 1966; Davis and Burchfiel, 1973) (Fig. 1). The tectonic role of the Garlock fault in accommodating relative plate motion between the Pacific and North American plates has puzzled geologists and remains unresolved (e.g., Hill and Dibblee, 1953; Davis and Burchfiel, 1973; McGill et al., 2009; Hatem and Dolan, 2018).

Several competing tectonic models have been developed to explain the evolution of the Garlock fault in the context of right-lateral Pacific-North America plate motion. The extrusion model (Hill and Dibblee, 1953) suggests that the Garlock fault is a conjugate structure to the right-slip San Andreas plate-boundary fault, such that synchronous slip on both structures extrudes the Mojave block to the southeast. This model predicts similar and constant slip rates along strike on both the San Andreas and Garlock faults (Fig. 2A). The transform-fault model (Hamilton and Myers, 1966; Davis and Burchfiel, 1973) suggests that the Garlock fault accommodates differential Basin and Range

extension, with greater west-directed extension north of the Mojave block driving the left-slip motion along the Garlock fault. This model makes no predictions for contractional deformation at the eastern terminus of the Garlock fault, nor for vertical-axis block rotations in the Mojave Domain (Fig. 2B). Lastly, the rotating-fault model (Garfunkel, 1974; Humphreys and Weldon, 1994; Platt and Becker, 2013) predicts clockwise rotation of the Garlock fault and its bounding wallrock to drive bookshelf faulting, with a decrease in slip magnitude toward each end of the fault, and termination structures coeval with motion along the Garlock fault (Fig. 2C).

The along-strike slip variation and termination history of the Garlock fault can provide important information to test models for its formation. To this end, the Avawatz Mountains are located at the eastern terminus of the Garlock fault where it intersects the NW-striking right-slip Southern Death Valley fault (SDVF) (Fig. 1, Fig 3). Jahns and Wright (1960) identified the Avawatz as the junction of the Garlock and SDVF, and proposed that the Avawatz Mountains had been uplifted 2.5 km. Hewett (1954, 1955), Jahns and Wright (1960), Hamilton and Myers (1966) and Brady (1986) suggested that the Garlock fault continues past the intersection with the SDVF before it terminates in the Avawatz Mountains.

Fortunately, these differing tectonic models for the Garlock fault generate different predictions for the kinematics and timing of deformation at the eastern fault terminus in the Avawatz Mountains (Fig. 2), making this range an ideal location to test proposed tectonic models for the Garlock fault and its role in accommodating relative plate motion.

Uplift of the Avawatz Mountains is possibly occurring along a contractional thrust belt related to the termination of the Garlock fault, a contractional left-step in the SDVF, or a combination of these two processes. If exhumation is due to a fault-termination thrust along the Garlock fault, then exhumation should be coeval with the initiation of sinistral slip along the Garlock fault between 11-18 Ma (Fig. 4A) (Burbank and Whister, 1987; Andrew et al., 2014; Sample, 2018). The Avawatz Mountains are located at a restraining bend in the SDVF where there is a left-step along the right-slip SDVF, this fault geometry would result in contractional deformation in the Avawatz Mountains (Fig. 4B). If exhumation is driven by transpression within a restraining bend along the SDVF, then exhumation in the Avawatz would be younger (<10 Ma), similar to the timing of major extension and dextral shear in Death Valley (Fig. 4B) (Holm et al., 1992; Holm and Dokka 1993; Bidgoli et al., 2018).

Previous work in the Avawatz Mountains by Reinert (2004) and Chinn (2013) applied apatite (U-Th)/He (AHe) and apatite fission track (AFT) thermochronology, but their results were inconclusive for interpreting when exhumation began. Reinert (2004) collected AHe and AFT samples from a ~1 km vertical transect across the eastern range front, proposing that tectonically induced cooling of the Avawatz Mountains had begun at ca. 4.8 Ma. Chinn (2013) conducted forward modeling on the AHe and AFT ages of Reinert (2004), and proposed a two-stage cooling model best-fits the data. These models suggest an increase in cooling rates from ~3 °C/Ma prior to 10 Ma to ~6 °C/Ma from 10 Ma until present (Chinn, 2013).

This study presents new geologic mapping and zircon (U-Th)/He thermochronology to provide new constraints on the timing of exhumation and to better understand the kinematics of deformation in the Avawatz Mountains. These new insights are used to address which model of exhumation best applies to the Avawatz Mountains, and to evaluate competing models for the origin and development of the Garlock fault.

## GEOLOGIC SETTING

### Garlock fault

The Garlock fault is a ~260 km-long, northeast-to-east striking, left-lateral fault that extends east from the San Andreas fault to its terminus in the Avawatz Mountains (Fig. 1). Various geologic features have been used to estimate cumulative left-lateral slip of 48 to 65 km along the Garlock fault (Smith, 1962; Davis and Burchfiel, 1973; Jahns et al., 1971). Smith (1962) related a northwest-trending Mesozoic dike swarm in the Spangler Hills north of the Garlock fault to a similar northwest-trending dike swarm in the Granite Mountains west of the Avawatz Mountains, estimating 64-km of left-slip along the Garlock fault. Smith and Ketner (1970) proposed 48 to 64 km of left-lateral offset of the Garlock formation from the Pilot Knob Valley to the El Paso Mountains (Fig. 1). Davis and Burchfiel (1973) relate the Layton Well thrust fault in the southern Slate Range from Smith and others (1968) to a thrust fault in the eastern Granite Mountains 13 km west of the junction between the Garlock fault and the SDVF. They interpret these thrust faults to be offset by 56 to 64 km of left-lateral slip along the

Garlock fault (Davis and Burchfiel, 1973). Jahns and others (1971) propose ~65 km of left-lateral offset of Paleozoic sedimentary rocks from the Panamint Range to the Avawatz Mountains.

Neotectonic slip rates are estimated to be 4.5-13 mm/yr along the Garlock fault (Fig. 1) (McGill and Sieh, 1993; McGill et al., 2009; Rittase et al., 2014). McGill and Sieh (1993) estimated Quaternary slip rates of 4-7 mm/yr near the El Paso Mountains, 4-9 mm/yr in Searles Valley, 3-9 mm/yr in Pilot Knob Valley, and 1-9 mm/yr in Leach Lake and the Avawatz Mountains (Fig. 1). McGill and others (2009) proposed a Holocene slip rate of ~7.6 mm/yr for the western Garlock fault at Clark Wash (Fig. 1). Rittase and others (2014) calculated a preferred Holocene slip rate of ~11-13 mm/yr for the central Garlock fault near Pilot Knob Valley (Fig. 1).

The initiation of sinistral faulting has been better constrained in the central and western segments of the Garlock fault (Fig. 1). In the El Paso Basin, Burbank and Whistler (1987) interpreted rotation of sedimentary units due to movement along the Garlock fault by ~10 Ma. Detrital zircon studies from El Paso Basin suggest sinistral slip on the Garlock fault had started by 12.5 Ma (Sample, 2018). Offset geologic markers in the Lava Mountains bracket the age of Garlock fault initiation to between 11.4 - 18 Ma (Andrew et al., 2014). Blythe and Longinotti (2013) interpret ca. 10 Ma exhumation in the Tehachapi Mountains to be related to the initiation of left-slip on the Garlock fault (Fig. 1).

Within the study area, the Garlock fault is expressed as the Leach Lake fault and the Mule Spring fault (Fig 5). The Mule Spring fault is the dominant fault

strand of the Garlock fault in the Avawatz Mountains and shows both left-lateral and dip-slip kinematics. The Mule Spring fault intersects the SDVF in the northern Avawatz Mountains near Sheep Creek (Fig. 5, Fig. 6). As this fault continues to the east, it displays more pronounced dip-slip kinematics, placing the Jurassic Avawatz monzodiorite complex over Neogene and Quaternary strata (Fig. 3, Fig. 5).

**Southern Death Valley fault zone**

The Southern Death Valley fault (SDVF) is a northwest-trending right-slip fault system from the southern end of Death Valley to the Avawatz Mountains (Wright and Troxel, 1967; Butler et al., 1988). This fault intersects the Garlock fault in the northern Avawatz Mountains (Fig. 1, Fig. 3, Fig. 5). Right-lateral shear in this area is due to the northwest-trending ECSZ that accommodates ~20-25% of the right-lateral motion between the Pacific-North American plates since its inception (Dokka and Travis, 1990; Miller et al., 2001). In the Death Valley region, this deformation is expressed as a pull-apart basin, with northwest-striking right-lateral strike slip faults, and southwest-striking normal faults (Burchfiel and Stewart, 1966; Stewart, 1983). The timing for the transition from Basin and Range extension to right-lateral transtension is debated, but studies suggest that in the Death Valley region this transition occurred ca. 10-6 Ma (Stewart, 1983; Holm and Dokka, 1991, 1992; Bidgoli et al., 2015; Fleming et al., 2021). Estimates for total displacement along this fault range from less than 8 km (Wright and Troxel, 1967) to up to 80 km (Stewart, 1983), however recent studies

suggests 30-40 km of right-lateral displacement along the SDVF (Butler et al., 1988; Pavlis and Trullenque, 2021).

In this study area the SDVF is exposed in the Noble Hills as five subparallel northwest-striking dextral strike-slip faults that place Neogene and Quaternary strata against crystalline basement and intrusive rocks (Fig. 5). These faults make a bend towards the east in the northern Avawatz Mountains as they intersect the Mule Spring branch of the Garlock fault (Fig. 5).

**Avawatz Mountains geology**

The Avawatz Mountains are in the northeastern corner of the Mojave Desert at the intersection of the Garlock fault and the SDVF (Fig. 1, Fig. 3). The core of the range is dominated by the heterogenous Jurassic Avawatz granodiorite complex, with additional Mesozoic intrusive rocks, and roof pendants of Proterozoic-Paleozoic siliciclastic and carbonate metasediments (Fig. 5). The range is flanked by Neogene terrestrial strata of the Military Canyon formation, Noble Hills assemblage, Arrastre Spring formation, and Avawatz formation (Henshaw, 1939; Spencer, 1981; Brady, 1986) (Fig. 5). The Neogene strata has been variably faulted and folded by deformation related to motion along the Garlock fault and SDVF (Spencer, 1981; Brady, 1984; Bidgoli, 2022) (Fig. 7A, 7B).

Exhumation of the Avawatz Mountains could be due to either a termination thrust related to the Garlock fault, or a restraining bend in the SDVF (Fig. 2, Fig. 4). An additional model has been proposed by [cite ref here] in which the

Avawatz Mountains were exhumed in the footwall of the Arrastre Spring normal fault on the southwest side of the range (Fig. 5). Spencer (1981) and Brady (1986) suggest motion along the Arrastre Spring fault occurred during the Neogene coeval with the deposition of the Arrastre Spring and Avawatz Formations. The Second Member of the Avawatz Formation buries the escarpment of the Arrastre Spring fault, constraining the age of the last motion along the fault (Spencer, 1981). The First Member of the Avawatz Formation has been dated to 20-21 Ma based on biotite K-Ar ages from tuff (Brady, 1986). Henshaw (1939) gave a Miocene to Pliocene age for Fourth Member of the Avawatz Formation based on fossil fauna. The upper member of the Avawatz Formation yielded biotite K-Ar ages of ca. 11 Ma (Everden et al., 1964). These existing age constraints indicate motion on the Arrastre Spring fault ceased prior to the 11 Ma.

Extensional events of a similar age have been observed north of the Garlock to the west in the Tehachapi Mountains and along the Sierra Nevada frontal fault (Blythe and Longinotti, 2013; Lee et al., 2023) (Fig 1).

The termination thrust model for the exhumation of the Avawatz predicts (1) primarily west-dipping, reverse faults, (2) exhumation ca. 18-11 Ma, coeval with estimates for Garlock initiation to the west (Burbank and Whistler, 1987; Blythe and Longinotti, 2013; Sample, 2018), and (3) rates and magnitudes of shortening recorded in the Avawatz be comparable to estimates along the Garlock fault (Fig. 4A). If the exhumation of the Avawatz is the result of a left-step in the SDVF it is predicted to have (1) complex restraining bend fault geometries

with approximately west -striking reverse faults and northwest to north-striking right-slip faults (Sanderson and Marchini (1984), (2) fault slip initiation ca. 10-8 Ma (Bidgoli et al., 2015; Sizemore et al., 2019), and (3) fault activity dominated by northwest-striking dextral faults rather than west-striking sinistral faults (Fig. 4B). It is possible the deformation from the SDVF has overprinted an original phase of deformation related to motion along the Garlock fault. In this case it may be possible to observe cross-cutting relations between structures, or changes in fault kinematics through time.

**Tectonic models for the Garlock fault**

The role of the Garlock fault in accommodating motion between the Pacific-North American plate has been widely debated (Hill and Dibblee, 1953; Hamilton and Myers, 1966; Troxel et al., 1972; Davis and Burchfield, 1973; Guest et al., 2003; McGill et al., 2009; Platt and Becker, 2013; Andrew et al., 2014; Hatem and Dolan, 2018). Three primary models have been proposed for the tectonic role of the Garlock fault (Fig. 2).

Hill and Dibblee (1953) interpreted the left-lateral Garlock fault as a conjugate shear to the right-lateral San Andreas fault (Fig. 2A). These conjugate faults accommodate the eastward translation of the Mojave block, which is caused by north-south compression resulting from the Big Bend in the dextral San Andreas fault (Stuart, 1991; Thatcher et al., 2016). The extrusion model predicts there to be constant magnitudes of slip along-strike for both the San Andreas and Garlock faults, and little to no contractional deformation at the

eastern terminus of the Garlock fault and no block rotation of the Mojave (Fig. 2A).

The transform fault model suggests the Garlock fault is accommodating differential extension between the western Basin and Range and the Mojave block (Hamilton and Myers,1966; Troxel et al., 1972; Davis and Burchfiel, 1973) (Fig. 2B). In this model the larger magnitude of extension in the Basin and Range north of the Mojave block is driving left-slip along the Garlock fault. This model is consistent with the location of the Garlock fault at the southern margin of the Basin and Range province, with major zones of extension restricted to the northern side of the Garlock fault. However, the modern extension direction in the Basin and Range province is towards the northwest (Dixon et al., 2000), nearly perpendicular to the northeast-east strike of the Garlock fault.

Recognition of the Eastern California Shear Zone (ECSZ) as a region of northwest-striking right-lateral shear extending both north and south of the Garlock fault (Dokka and Travis, 1990; Schermer et al., 1996; Miller et al., 2001 Oskin et al., 2008) makes it difficult to explain the Garlock fault as an accommodation structure between two separate tectonic regimes. This has led to the development of the rotating fault model in which the entire Garlock originally had the 060$^{o}$ strike as present-day western segment, and that the central and eastern portions were rotated clockwise into their present-day orientation (Guest et al., 2003; McGill et al., 2009; Platt and Becker, 2013; Andrew et al., 2014; Hatem and Dolan, 2018) (Fig. 2C).

## GEOLOGIC MAPPING OF THE AVAWATZ MOUNTAINS

Geologic mapping was conducted at a 1:24,000 scale to better understand the late Cenozoic deformation of the Avawatz Mountains (Fig. 5). Mapping was completed using field observations, NAIP satellite imagery, 10m and 0.5m Digital Elevation Models (DEMs), and previously published maps (Spencer, 1981; Brady, 1986; Miller et al., 2014). Field-based mapping was conducted on an iPad mini using the mobile GIS software platform FieldMove to collect observations and fault orientation and kinematic data defined by slickenlines on fault surfaces. Geologic units in this map are those defined by Spencer (1981) and Brady (1986). In the office, ArcMap and QGIS were used to construct base maps and draft map topology. Rock samples were collected for geochronologic, geochemical, and petrographic analyses to characterize and differentiate the various igneous intrusions throughout the range (Fig. 5). A detailed map of the northern Avawatz Mountains will be published through the USGS EdMap program.

### Geologic Units

#### *Precambrian and Paleozoic rocks*

The oldest unit in this area is Proterozoic basement gneiss that is in a structural block north of the Mule Spring fault (Fig. 5). This gneiss is heterogenous but generally has porphyroclasts of plagioclase and quartz up to 1 cm and weak-to-strong foliations defined be aligned biotite. In some exposures porphyroclasts are k-feldspars, but in most outcrops k-feldspar is absent or in

minor concentrations. This gneiss is similar to exposures described to the north in Death Valley (Lima et al., 2018).

There is an unconformable depositional contact between the gneiss and overlying Precambrian sediments of the Pahrump Group (Wright and Troxel, 1966; Brady, 1986). This group contains the Crystal Spring Formation, Beck Spring Dolomite, and the Kingston Peak Formation. In the Avawatz only the Crystal Spring Formation and Kingston Peak Formation appear with certainty (Wright and Troxel, 1966; Brady, 1986). A dolomite unit correlative to the Beck Spring Dolomite has not been recognized in the Avawatz. However, previous mapping recognized tens of meters of dolomite in the upper Crystal Spring Formation that could be a thin, poorly developed section of the Beck Spring Dolomite (Troxel and Butler, 1979).

These units have been weakly metamorphosed in the Avawatz Mountains, but they still retain their primary sedimentary structures such as cross-beds. The Crystal Spring Formation includes beds of fine-grained quartzite, coarse-grained metasediments, and minor dolomite and chert beds. Precambrian gabbro sills have intruded the Crystal Spring Formation altering dolomite beds to Talc (Brady, 1986) (Fig. 7C). Similar intrusions in the Crystal Spring Formation can be found around the Death Valley region (Heaman and Grotzinger, 1992).

The Kingston Peak Formation found in the Avawatz Mountains has previously been correlated to the southern facies of the Kingston Peak Formation (Troxel, 1967; Brady, 1986). This unit contains diamictite with fine to coarse grained clasts of quartzite and granite in a fine-grained matrix (Brady, 1986).

Regionally these diamictites have been used as evidence for global glaciation event during the Neoproterozoic (Miller, 1985; Le Heron et al., 2014). The sediments of the Pahrump Group were deposited in the Amargosa aulacogen that formed during the Neoproterozoic rifting of Rodinia (Wright et al., 1974).

Through the Neoproterozoic and Paleozoic, passive margin sediments were deposited over the rocks of the Pahrump Group. This includes the Precambrian Noonday Dolomite, Johnnie Formation, and Stirling Quartzite; the Cambrian Wood Canyon Formation, Zabrinske Quartzite, Carrara Formation, Bonanza King Formation, and the Nopah Formation. Sedimentation continued with the deposition of the Devonian Sultan Limestone, the Mississippian Monte Cristo Limestone, and the Pennsylvanian-Permian Bird Spring Formation.

These passive margin sedimentary rocks are not exposed as a coherent and conformable stratigraphic section, but are rather found as roof pendants within Mesozoic plutons in the Avawatz Mountains (Fig. 5). Previous mapping by Brady (1986) identified ~1km of these Precambrian to Paleozoic rocks as roof pendants in Mesozoic intrusive rocks in the central Avawatz Mountains (Fig. 5).

For our mapping purposes, some of these units are grouped together because identification of individual formations is not always possible. The Crystal Spring Formation and Kingston Peak formation are grouped as undifferentiated rocks of the Pahrump Group (Fig. 5). The Precambrian and early Cambrian rocks of the Noonday Dolomite, Johnnie Formation, Stirling Quartzite, Wood Canyon Formation and Zabriskie Quartzite are grouped together as undifferentiated later Precambrian and Cambrian rocks because they are

dominantly medium-to-fine grained siliciclastic rocks that have been metamorphosed by Mesozoic intrusions (Fig. 5). The remaining Paleozoic carbonate units of the Carrara Formation, Bonanza King Formation, Nopah Formation, Sultan Limestone, Monte Cristo Limestone, and the Bird Spring Formation are grouped as undifferentiated Paleozoic carbonate rocks since they have been mostly metamorphosed into massive marble units (Fig. 5).

### *Mesozoic rocks*

Mesozoic metasedimentary and metavolcanic rocks found southwest of the Avawatz in the Fort Irwin Army Base and were unable to be examined during mapping efforts (Fig. 5). Descriptions and locations of this rock are based on previous research in the area (Spencer, 1981; Brady, 1986). These rocks outcrop west of the Arrastre Spring fault and are not found in the core of the Avawatz Mountains. Brady (1986) described these rocks as being pale-colored phyllite and schist with moderately to strongly developed schistosity. They contain quartz porphyroblasts but lack any mafic clasts. They have been interpreted to be from rhyolitic tuffs and flows that have been experienced low greenschist grade metamorphism (Brady, 1986).

The dominant lithologies in the Avawatz range are a series of Mesozoic intrusive rocks (Fig. 5). The oldest of these is the Granite of Avawatz Peak that intrudes into Paleozoic carbonate rocks. In the western Avawatz this granite is later intruded by the Cave Spring monzonite, previously mapped by Spencer (1981) as the quartz monzonite of Cave Spring (Fig. 5). This unit appears to have

an intrusive contact with the Granite of Avawatz Peak and older Paleozoic carbonate unit (Fig.5). The most extensive unit in the area is the Jurassic Avawatz granodiorite complex that forms the bulk of the range (Fig. 5). This unit intrudes both younger intrusive units and has large pendants of Precambrian siliciclastic rocks and Paleozoic carbonates. A younger granodiorite intrusion is exposed west of Mormon Spring (Fig. 5).

There are additional Mesozoic intrusions north of the Mule Spring fault (Fig. 5). The largest of these is of similar composition to the Avawatz granodiorite complex but intrudes into Paleozoic gneiss and not siliciclastic sediments (Fig. 5). This unit was not directly dated but is likely Jurassic or Cretaceous in age. A younger Cretaceous granite intrudes this unit and is exposed over a large area north of the Mule Spring fault (Fig. 5). Previous research has related these intrusions to similar aged intrusions northwest of the Avawatz in the Owlshead Mountains (Pavlis and Trullenque, 2021).

***Cenozoic rocks***

Neogene terrestrial sedimentary and volcanic units were deposited in basins throughout this region (Spencer, 1990). The Noble Hills assemblage is located in the northwest portion of the map area and was named and described in detail by Brady (1986) (Fig. 5). It is exposed in fault blocks of the SDVF where it is juxtaposed against Mesozoic intrusive rocks and Proterozoic basement gneiss (Fig. 5). This unit contains terrestrial volcaniclastic rock, ashfall tuff, and abundant fine-grained sediments. Megabreccia layers in this unit interbedded

with fine grained lacustrine sediments suggests this unit was deposited in an active tectonic environment. The basal unit of the Noble Hills assemblage is a series of landslide breccia deposits that was interpreted by Brady (1986) to be in depositional contact with the lower portion of the Noble Hills assemblage. This unit contains large 30 m-wide blocks of weakly metamorphosed Kingston Peak and Crystal Springs formations that were previously interpreted to have been sourced from similar rocks exposed in the Avawatz Mountains (Brady, 1986). Previous research has suggested that the blocks are preserved in reverse stratigraphic order, indicating the source of these blocks was being denuded and exposing progressively older units (Troxel and Butler, 1979; Brady 1986).

The Military Canyon Formation was described in detail by Brady (1986). This unit outcrops along the north side of the Mule Spring fault and extends as a thin fault bound body to the intersection of the SDVF (Fig. 5). The lowest exposed member contains a coarse-grained conglomerate that is faulted against Mesozoic intrusive rocks and units of the Noble Hill assemblage (Fig. 5). The middle member records a fining upward sequence from coarse conglomerate to thinly bedded sandstone and siltstone. The upper member contains conglomerates fining upward to fine-grained sandstone and eventually beds of gypsum and halite. Brady (1986) interpreted the fining-upward and thinning of younger units to record tectonically-induced changes in the depositional environments of these units. Brady (1986) suggests the Military Canyon Formation is younger than ca. 12 Ma andesitic volcanism in the Owlshead Mountains and is likely Pliocene in age.

The Arrastre Spring Formation was named by Spencer (1981), and outcrops as deformed bodies along the Arrastre Spring fault in the southwest Avawatz (Fig. 5). This unit is dominated by matrix-supported conglomerate, with some siltstone, volcanic breccias and minor volcanic flows (Spencer, 1981; Brady, 1986). Spencer (1981) suggests the Arrastre Spring Formation is middle Miocene or younger, and Brady (1986) reports 12-13 Ma ages for silicic volcanic rocks from the lower Arrastre Spring Formation. However, it is not clear what mineral or system was used to obtain these ages (Brady, 1986).

This unit was not directly mapped in the field due to its location in the Fort Irwin Army Base. Descriptions and the location of this unit are based on previous studies by Spencer (1981) and Brady (1986).

The Avawatz Formation was first recognized and named by Henshaw (1939) and was later described by Spencer (1981) and Brady (1986). This unit is exposed in the southern portion of the range (Fig. 5), and as an isolated body within the Avawatz Mountains. Spencer (1981) divided this formation into four members, but for this study they will be grouped as a single unit. A small portion of this unit is deposited within this map area. This unit was deposited unconformable against Mesozoic intrusive rocks and Precambrian to Paleozoic sedimentary rocks, suggesting there was a period of deformation prior to the Neogene resulting in the tilting and exposure of multiple structural levels within the proto Avawatz Mountains. The lower members of the Avawatz formation contain granitic and gneissic clasts determined to have been sourced from the northeast, while the upper members contain metavolcanic and carbonate rocks

that were interpreted to have been sourced from the south (Spencer, 1981; Brady, 1986). In total this unit is about 3000 m thick and shows thickening of the unit to the west. This unit has been interpreted to have formed in a basin bound by the west dipping Arrastre Spring fault. Previous mapping has identified that second member buries the Arrastre Spring fault, suggesting this fault may have not been active during the deposition of the entire formation (Spencer, 1981).

## GEOLOGIC OBSERVATIONS

In the northwest portion of the map area, the Neogene Noble Hills assemblage outcrops as low foothills northwest of the main Avawatz Mountains (Fig. 5). This unit is composed of terrestrial clastic sediments, with minor volcanic tuffs and volcaniclastic sediments. This unit appears to be in depositional contact with a Neogene landslide breccia unit described by Spencer (1981) and Brady (1986). This landslide breccia contains large 30 m-wide blocks of weakly metamorphosed Crystal Springs and Kingston Peak formations that area found in the vicinity of Sheep Creek. For this study, these two units are combined as the Noble Hills assemblage because there does not appear to be a fault contact between the two units.

The northern strand of the SDVF is at the range front of the Noble Hills (Fig. 5). This fault is concealed in the youngest alluvium but appears to offset the surface of an intermediate Quaternary fan (Fig. 5). This fault becomes difficult to trace to the east as it appears to cut into the Neogene landslide breccia before being concealed by the youngest alluvium.

South of this fault is a large block of the Noble Hills assemblage dominated by fine grained clastic sediments and evaporite deposits that have been tightly folded near fault zones (Fig. 5., Fig. 7A, Fig. 7B). These folded sediments are well exposed in Ws (Fig. 6). Fold hinge measurements of 04/298 and 06/100 indicate these folds are oriented west-northwest with gentle plunges (Fig. 7B).

A northwest-striking right-slip fault juxtaposes the northeast block of the Noble Hills assemblage against the central fault block (Fig. 5). This fault produces a damage zone of ~10 meters on either side of the fault where rocks are highly fractured with subvertical fracture orientations. A secondary fault associated with the main fault trace has a strike of 316° with a dip of 87° to the north. The main fault strand offsets the surface of an intermediate Quaternary fan near Pipeline Wash (Fig. 5. Fig. 6). The central fault block is composed of Proterozoic gneiss that has been intruded by Cretaceous granite. These rocks are restricted to north of the Mule Spring fault but extend across the range front to the east (Fig. 5).

The central fault block is faulted against the Noble Hills assemblage again by a northwest-striking right-slip fault (Fig. 5). The southern Noble Hills fault block generally contains coarse grain sized compared to the northern fault block. There is abundant red to purple sandstone and mudstone beds, and a distinct layer of volcaniclastics with large clasts of extrusive volcanic rocks. Bedding measurements from Amphitheater show the strike of beds varies from 83° to 116°, with dips from ~60-80 degrees south. The bedding in this block displays

consistent dips to the south and is less intensely folded than the northern block of the Noble Hills assemblage. The most recognizable unit in this block is a 5-10 m thick bed of coarse-grained conglomerate composed of subangular to angular granitic clasts. This bed is used to correlate outcrops of the Noble Hills assemblage further to the east (Fig. 5). It is well exposed in Amphitheater Wash where it forms large flat irons dipping to the south (Fig. 6).

The fourth trace of the SDVF juxtaposes the southern block of the Noble Hills assemblage against the Neogene Military Canyon formation (Fig. 5). This fault is a northwest-striking right-slip fault in Pipeline Wash, but to the east it is expressed as a west-striking fault in Amphitheater Wash (Fig. 5, Fig. 6). A related secondary fault in Amphitheater is striking 95° with a dip of 84° to the south. The western trace of this fault is covered by the oldest Quaternary alluvium, and this fault does not appear to cut any of the Quaternary surfaces (Fig. 5).

Within the Military Canyon formation there is a noticeable change in bedding orientations. In Pipeline Wash just north of the Mule Spring fault, the bedding of a conglomerate bed is striking 241° dipping 75° to the northwest (Fig. 6). In Amphitheater Wash bedding of a similar conglomerate bed is striking 234° dipping 37° to the northwest (Fig. 6). The sedimentary units within the Military Canyon formation are generally more coarse-grained than the sediments in the Noble Hills assemblage. In this area the Military Canyon formation is dominated by conglomerates but displays an overall fining upwards into fine-grained sandstone and mudstone with evaporites. A small fault block of the Military Canyon formation is bounded by the fourth trace of the SDVF and the Mule

Spring fault (Fig. 5). This block extends to the east towards Sheep Creek before it appears to be pinched out between the Mule Spring fault and other traces of the SDVF (Fig. 5, Fig. 6). Field mapping did not identify any exposures of the Military Canyon formation further to the east (Fig. 5).

In the western map area, the Mule Spring fault displaces the Jurassic Avawatz granodiorite complex against the Military Canyon formation (Fig. 5, Fig. 7D). This fault is exposed west of Pipeline Wash and at the head of Amphitheater Wash (Fig. 5, Fig. 6). West of Pipeline Wash, the main trace of the Mule Spring fault is striking 81° dipping 60° to the south (Fig. 6). Up to ~50m south of the fault, the Avawatz granodiorite is highly fractured with subvertical fractures producing a scaly texture in the rocks. This fracture orientation is roughly parallel to the trace of the Mule Spring fault. In the field, this fault trace is cutting vertically across drainages, suggesting the fault is dipping near vertically (Fig. 7D). There are no clear kinematic indicators on these faults. The Mule Spring fault does not appear to offset any of the Quaternary surfaces along the trace of the fault in the western Avawatz (Fig. 5).

South of the Mule Spring fault, the Avawatz granodiorite is in intrusive contact with Paleozoic carbonates (Fig. 5). This contact is irregular, and extends to the east, south of the trace of the Mule Spring fault. This contact is later intruded by the monzonite of Cave Spring (Fig. 5). It is possible this contact is a fault contact: there are several fault planes exposed in a wash with orientations of 088/63 south, 131/58 southwest, and 300/89 northeast. Due to the similar rock

types, it was difficult to determine if these faults were significant structures, or just minor faults within the intrusions.

This unit extends eastward into the Avawatz Mountains where it appears to be faulted against the Avawatz granodiorite by the eastern extent of the Leach Lake fault (Fig. 5). To the west, the Leach Lake fault appears to have scarps in all three Quaternary units. Southern splays of this fault also cut Quaternary fan surfaces (Fig. 5).

The area to the southwest was not visited in the field during this study due to its location within the Fort Irwin Army Base. Mapping was completed in this area using NAIP imagery, hillshades derived from 0.5m LIDAR DEMs, and previous mapping in this area by Spencer (1981) and Brady (1986).

The Proterozoic Crystal Spring formation is exposed at the mouth of Sheep Creek (Fig. 5, Fig. 6, Fig. 7C). This unit has been weakly metamorphosed but retains primary sedimentary bedding and sedimentary structures such as cross beds. In this location bedding is steeply dipping to the north and south (266/85 north, 111/86 south) and is locally overturned. The Crystal Spring formation has been intruded by a gabbro (Fig. 8), that has altered dolomite beds to talc. There are several faults cutting that Crystal Spring formation that are likely unrelated to Cenozoic deformation since they do not appear to cut any units other that the Crystal Spring formation (Fig. 5). Outcrops of the Kingston Peak formation are seen in washes east of Sheep Creek. These units are coarser-grained than metasediments of the Crystal Spring formation. The Pahrump Group outcrops further to the east near Avawatz Canyon where it is

faulted against the Noble Hills assemblage (Fig. 5). This fault is exposed in the wash east of Anvil Canyon, where the fault plane is striking 103° and dipping 71° to the southwest (Fig. 5). In the northwest corner of the map area the Kingston Peak formation of the Pahrump group is exposed in a continuous stratigraphic section. This unit is weakly metamorphosed but preserves primary sedimentary structures. This unit alternated from fine-grained to coarse-grained metasediments. Some outcrops show 20-30 cm-wide clasts of quartzite that have deflected lower beds and are draped by younger sediments. This unit is in fault contact with Precambrian to Cambrian quartzites. Both these units have been intruded by a Cretaceous granite that is similar to granite exposed in Anvil Canyon (Fig. 5).

Near Sheep Creek, the Pahrump group is in depositional contact with Proterozoic basement gneiss (Fig. 5, Fig. 6). This contact extends to the southwest where it is cut by a strand of the SDVF (Fig. 5). The basement gneiss has porphyroclasts of plagioclase and quartz up to 1cm with weak-to-strong foliation defined by biotite. To the east the gneiss has an augen texture with 1cm porphyroclasts of potassium feldspar. Exposures of the gneiss are restricted to the northeast of the SDVF and north of the Mule Spring fault (Fig. 5, Fig. 6). The gneiss exposed in the central block of the SDVF appears to be the same as the gneiss near Sheep Creek (Fig. 8). Southwest of Sheep Creek the gneiss is intruded by a Mesozoic diorite (Fig. 5). This unit is not aerially extensive and was mapped as a separate unit from the Avawatz granodiorite complex because it is found north of the Mule Spring fault (Fig. 5). In outcrop appears to have less

amphibole than the Avawatz granodiorite. The gneiss and diorite are both intruded by a Cretaceous granite (Fig. 5). This granite contains quartz, plagioclase, potassium feldspar, mica with accessory garnets. It is restricted to the northern side of the Mule Spring fault and is found in the central fault block of the SDVF where it is in intrusive contact with the Proterozoic gneiss (Fig. 5). The Cretaceous granite is observed to be in fault contact with the Noble Hills assemblage across the northern Avawatz Mountains (Fig. 5).

South of the Mule Spring fault, the Jurassic Avawatz granodiorite complex makes up the bulk of the range (Fig. 5). This unit has varying compositions (Fig. 8), but the bulk composition is plagioclase, hornblende, quartz, and biotite. Epidote alteration is common near fault zones and younger intrusive dikes. Aplite dikes are commonly cutting the granodiorite complex. The Jurassic Avawatz granodiorite complex intruded the older granite of Avawatz Peak, and the Jurassic monzonite of Cave Spring (Fig. 5). The intrusive contact with the monzonite is seen in the western map area (Fig. 5). The intrusive contact with the granite of Avawatz Peak is irregular and can be seen in the interior of the range (Fig. 5). Smaller pendants of the granite can be found in the granodiorite in the western portion of the range (Fig. 5). There are abundant pendants of Precambrian to Cambrian sedimentary units within the Avawatz granodiorite (Fig. 5). Paleozoic carbonates make up most of the pendants in this map area (Fig. 5). These are best exposed in the core of the range west of Mormon Spring, and just south of the Mule Spring fault (Fig. 5). Primary sedimentary structures are preserved within the Paleozoic carbonates in the core of the range. Based on

observations of mapping completed by Spencer (1986) the Avawatz granodiorite intruded up through at least the Devonian Sultan limestone. A younger Mesozoic monzonite intrusion is seen within the Jurassic Avawatz granodiorite west of Mormon Spring (Fig. 5). This unit is observed to have many dikes radiating outward from the intrusion into the Avawatz granodiorite. Smaller bodies of this unit are observed in the northwest (Fig. 5).

Along the eastern range front, the Mule Spring fault places the Jurassic Avawatz granodiorite over intermediate Quaternary fans and the Neogene Noble Hills assemblage (Fig. 5, Fig. 9). Where exposed north of Mormon Spring the fault strikes 184° dipping 41° to the west, placing the Avawatz granodiorite over intermediate Quaternary fans (Fig. 9A). Further to the north this fault is observed to be striking 137° with a dip of 34° to the southwest (Fig. 9B). Slickenlines on this fault surface are plunging towards 198° (Fig. 9B). In this location the fault is placing the Avawatz granodiorite over Neogene sediments (Fig. 5, Fig. 9B). The Neogene unit is interpreted to be the Noble Hills assemblage due to the identification of a coarse-granite granite conglomerate unit that is similar to a unit observed in the Noble Hills assemblage to the west. South of Mormon Spring the fault juxtaposes the Avawatz granodiorite complex on either side (Fig. 5).

## STRUCTURES

### Southern Death Valley fault (SDVF)

The Southern Death Valley fault (SDVF) is expressed as a ~2.5-km-wide zone of northwest-striking subvertical right-lateral strike slip faults (Fig. 5). Field

mapping identified at least four subparallel fault strands that juxtapose crystalline rocks and Neogene strata of the Noble Hills assemblage (Fig. 5).

The first strand lies at the northeast range front of the Noble Hills, where a Neogene landslide complex has an abrupt contact with Quaternary alluvium. This fault is not expressed in the youngest alluvium but appears to cut the surface of an older Quaternary fan suggesting it has been active in the Quaternary (Fig. 5). In this fault block the beds in the Noble Hills assemblage are highly deformed with west-trending fold axes. Near fault zones, evaporite beds are often tightly folded (Fig. 7A, Fig. 7B).

The second strand displaces the Noble Hills assemblage against Mesozoic intrusive crystalline rocks and Precambrian basement gneiss (Fig. 5). Rocks from this fault block appear to extend across the northern Avawatz Mountains and are exposed near Sheep Creek (Fig. 5, Fig. 6). A secondary fault associated with this strand has a strike of 300° and dips 88° northeast.

The third strand displaces Mesozoic crystalline rocks and Precambrian gneiss against Neogene terrestrial sediments of the Noble Hills assemblage (Fig. 5). This block includes Neogene volcanics and clastic sediments.

The fourth and southernmost strand displaces the Neogene Noble Hills assemblage against the Neogene Military Canyon formation (Fig. 5). Both units are of similar age and were likely deposited in similar depositional environments. The Military Canyon formation in this area is dominated by conglomerates and has a larger grain size than the rocks in the Noble Hills assemblage.

Several of these fault traces continue to the southeast where they displace Neogene sediments against Mesozoic crystalline rocks and Precambrian gneiss (Fig. 5). The eastward bend in these faults suggest that they could have been deflected because of left-lateral slip along the Mule Spring fault.

**Garlock fault zone**

The Mule Spring branch of the Garlock fault is the dominant fault strand in this area (Fig. 5, Fig. 6). In the western portion of the map, the fault is striking 98° dipping 77° to the south. It displaces the Jurassic monzodiorite against Neogene conglomerates of the Military Canyon Formation (Fig. 5, Fig. 7D). A secondary fault within the monzodiorite has a strike of 282° dipping 81° north, with slickenlines plunging 6° towards 101°.

Near the junction with the SDVF the Mule Spring fault begins to dip slightly towards the south and displays stronger dip-slip fault kinematics. In this area the Mule Spring fault appears to override and truncate the southern trace of the SDVF (Fig. 5). The increased southern dip can be seen as the fault “V’s” south up drainages indicating a southward dip of the fault surface (Fig. 5). This is best expressed at the head of Anvil Canyon where the trace of the Mule Spring fault “V’s” to the southwest into the Avawatz, suggesting it is dipping to the south-southwest in this location (Fig. 5). Through the northern portion of the Avawatz Mountains the Mule Spring fault continues to thrust Jurassic monzodiorite over Neogene terrestrial sediments (Fig. 5).

The Leach Lake fault is a sub-parallel strand of the Garlock fault south of the Mule Spring fault in the western map area (Fig. 5, Fig. 6). This fault displaces the Jurassic monzodiorite complex against Jurassic-Triassic metavolcanics and metasediments (Fig. 5). This region was unable to be reached in field mapping due to its location in the Fort Irwin Army Base. Field relationships were taken from Spencer (1981) and Brady (1986), and observation in 0.5m LiDAR derived DEMs. This strand of the fault offsets Quaternary fan surfaces indicating that it is an active Quaternary fault (Fig. 5). This fault appears to branch to the east. The northern strand continues into bedrock where it was difficult to map because of similar Mesozoic intrusions on either side of the fault (Fig. 5). The Southern strand appears to bend southward where it could merge with the Arrastre Spring fault (Fig. 5).

Stereonets of faults within the Garlock fault zone show most faults are west-striking with strike-slip kinematic indicators (Fig. 10A). Near the intersection with the SDVF fault orientations are more variable, and dip-slip slickenlines are common (Fig. 10B).

**Eastern Mule Spring fault**

Along the eastern range front the Mule Spring fault makes a bend to the south as a west-dipping reverse fault (Fig. 5). Several exposures can be seen where the fault is displacing the Jurassic monzodiorite over Neogene to Quaternary sediments (Fig 5, Fig. 9). North of Mormon Spring the fault is striking 184° dipping 41° to the west, placing the Avawatz granodiorite over intermediate

Quaternary fans (Fig. 9A). Further to the north this fault is observed to be striking 137° with a dip of 34° (Fig. 9B). Slickenlines on this fault surface are plunging towards 198°. Slickenlines on this fault plane show dip-slip kinematics (Fig. 9B). South of Mormon Spring the hanging wall and footwall of this fault are both Jurassic granodiorite (Fig. 5). The fault splays into two subparallel faults. A secondary fault associated with one of these splays has a strike of 156° dipping 32° to the west.

The surface of an intermediate Quaternary fan ~1km east of the Mule Spring fault is warped with a ~20 m tall scarp (Fig. 5). Despite this significant deflection of the fan surface, no clear Quaternary scarps cut the fan surface (Fig. 5). This warped surface extends to the northwest outboard of the range front towards Sheep Creek (Fig. 5, Fig. 6). Quaternary fans south of this mapped fault are more heavily incised than those north of the fault suggesting the southwestern side of the fault is being uplifted relative to the northeast side (Fig. 5). The inferred kinematics of the concealed fault are a west-southwest dipping reverse fault. It is possible this fault I kinematically linked with the Mule Spring fault.

**Arrastre Spring fault**

The Arrastre Spring fault is a Neogene age normal-oblique fault on the southwest side of the Avawatz Mountains (Fig. 5, Fig. 6). This fault was not observed directly during field mapping due to its location within the Fort Irwin Army Base. The location of this fault was determined based on mapping by

Spencer (1981) and Brady (1986). This fault cuts Mesozoic intrusive units and Precambrian to Paleozoic pendants within the intrusive units. The Neogene Arrastre Spring formation is deposited along the trace of the fault. In the southern map area this unit is observed to be deposited over the trace of the fault. Previous K-Ar ages from this unit give an age of 20-11 Ma (Spencer, 1981).

## ANALYTICAL METHODS AND RESULTS

### (U-Th)/He Thermochronology Methods

(U-Th)/He thermochronology utilizes the accumulation of $^{4}He$ in minerals due to the radioactive decay of U, Th, and Sm. During alpha decay of the parent nuclide (U,Th,Sm), $^{4}He$ can be produced as a result of the ejection of alpha particles. When minerals are above their closure temperature, the rate of $^{4}He$ diffusion is greater than the rate of alpha decay and $^{4}He$ production, and therefore there is no $^{4}He$ retained in the crystal. Once a mineral cools below its closure temperature, the rate of $^{4}He$ diffusion is no longer greater than the rate of alpha decay, and the $^{4}He$ produced in the crystal is retained within the grain. The exact closure temperature can vary depending on radiation damage to the grain, composition of the grain, cracks, or other physical damage to the grain. (Anderson et al., 2017). As a result, there is a range of closure temperatures dubbed the partial retention zone (PRZ), where some, but not all, $^{4}He$ could still be diffusing from the grain. The zircon (U-Th)/He PRZ is from ~140-200$^{o}$C (Reiners et al., 2004; Guenthner et al., 2013), while the apatite (U-Th)/He PRZ is typically from 55-80$^{o}$C (Farley, 2000). The application of these

thermochronometers can track the thermal history of a sample from ~200°C to 60°C during exhumation in the shallow crust. I conducted zircon and apatite (U-Th)/He thermochronology to better constrain the low-temperature cooling history of these rocks. Evidence of an exhumed fossil PRZ or PAZ would provide a time-constraint for when the sample was last at a temperature greater than the PRZ or PAZ.

Ten samples of Mesozoic crystalline rocks were collected from a ~1 km vertical transect in the hanging wall of the Mule Spring fault for zircon and apatite (U-Th)/He thermochronology (Fig. 5). Samples were collected at the same location as a previous study from Reinert (2004) which conducted AHe and AFT analyses. Reinert (2004) proposed that reverse slip began ca. 4.8 Ma along a hypothesized west-dipping fault west of the currently active range front reverse fault. However, the results do not fully capture the exhumation of the fossil AHe PRZ or the fossil AFT PAZ (Reinert, 2004).

Whole rocks were processed using a jaw crusher, followed by a cone crusher, then sieved to select grains <355 μm. These grains were washed in a beaker to remove fines, then dried on a hot plate at <100°C. Magnetic grains were removed using a handheld magnet before being passed through a Frantz magnetic separator at 0.5 A, 1 A, and 1.6 A. Apatite grains were collected from 4 samples by processing the nonmagnetic grains in lithium metatungstate (density = 2.7 g/mL) to concentrate apatite (density = 3.0 g/mL) and zircon (density =4.6 g/mL). Grains with a density >2.7 g/mL were then processed in methylene iodide (density = 3.2 g/mL) to separate zircon from apatite. In the six samples where

only zircons were collected, all nonmagnetic grains were processed only through methylene iodide. Zircon and apatite grains were taken to the CuTRaIL lab at the University of Colorado, Boulder for analyses. For each sample, 3-5 grains were selected, imaged and measured before being packed into Nb metal packets for (U/Th)/He analyses.

Helium concentrations were measured at CuTRaIL using an ASI Alphachron. Samples are heated using a diode laser, spiked with $^{3}He$, and measured on a Pfeiffer Balzers QMS quadrupole mass spectrometer. U and Th concentrations were measured by dissolving samples in hydrofluoric acid and analyzing using an Agilent 7900 Quadrupole inductively coupled plasma mass spectrometer (ICP-MS) with an Agilent SPS4 autosampler.

**(U-Th)/He Results**

A complete summary of apatite and zircon (U-Th)/He data is shown in Table 1. Complete data tables are provided in the Appendix (Table A1, Table A2). At least three grains were analyzed from every sample, except WJ 11-13-21-04 in which five zircons were analyzed. The age of these samples reflects when they cooled below the closure temperature depending on the decay system and mineral being analyzed. For most samples analyzed, the range of aliquot ages was less than 4 Ma (Fig. 11). Sample WJ 1-10-22-01 is from the highest elevation and exhibits the largest spread in aliquot ages from 67.1 Ma to 87.2 Ma (Fig. 11, Table A1). This sample has a slight positive correlation between age and effective uranium (eU) concentration, with the older two grains having higher

eU than the younger grain (Table A1). Sample WJ 11-13-21-04 was collected from the Mormon Canyon monzonite. Five grains from this sample were analyzed with He ages ranging from 7.6 to 20.2 Ma (Fig. 11, Table A1).

Zircon (U-Th)/He mean ages from ten samples have mean corrected He ages ranging from 12.3 ± 3.1 Ma to 79.4 ± 10.8 Ma (Fig. 11, Table 1). If the two oldest ages are excluded, the mean age from the eight youngest samples cluster around 15 Ma. Sample ages generally increase with increased elevation (Fig. 11).

New apatite (U-Th)/He ages from four samples yield mean He ages from 3.7 ± 0.3 Ma to 7.1 ± 0.1 Ma (Table A2). When combined with existing apatite (U-Th)/He ages from Reinert (2004), mean He ages range from 4.8 ± 0.6 Ma to 7.2 ± 1.0 Ma (Fig. 12). Apatite He ages do not show a strong trend of increasing age with elevation compared with zircon He ages (Fig. 13). The lowest elevation samples have similar ages to the highest elevation samples (Fig. 12, Fig. 13).

Zircon He ages generally increase westward from the range front, and the sample age is generally increasing with increased elevation (Fig. 14).

**U-Pb Zircon Geochronology Methods**

I employed U-Pb zircon geochronology to determine the crystallization age of igneous rocks and the detrital zircon signal of Proterozoic-Paleozoic basement rocks to better establish their age and stratigraphic correlations. Zircon grains were separated using the zircon separation method outlined for the (U-Th)/He methods. For igneous dating, zircon separates were sent to the Nevada Plasma

Facility Laboratory at the University of Nevada, Las Vegas where grains were hand-picked and mounted on double sided tape on 2.5 cm diameter acrylic mounts and laser spots were chosen targeting non-broken, inclusion-free grains. Analysis was conducted by laser ablation-inductively coupled plasma-mass spectrometry (LA-ICP-MS) to determine zircon U-Pb ages. Sample mounts were loaded into a TwoVol 1 ablation cell and ablated using an ESL 193 nm NWR193 excimer laser for analysis with a Quadrupole collector ThermoFisher Scientific TM iCAP ICP-MS at the Nevada Plasma Facility Lab at the University of Nevada, Las Vegas. Corrections for depth-dependent elemental and isotopic fractionation were performed using zircon standards FC1 (1099 ± 0.5 Ma; Paces and Miller, 1993), and secondary standard Fish Canyon Tuff zircon (27.65±0.34 Ma; Lanphere and Baadsgaard, 2001) to monitor data quality. A primary standard was analyzed for every five unknown analysis and one secondary standard was analyzed for every fifteen unknown analyses. Zircon analyses were reduced using the VizualAge™ workflow in the Iolite™ plugin for Igor Pro™ (Paton et al., 2010; Paton et al., 2011; Petrus and Kamber, 2012). To constrain the crystallization age of igneous samples, I calculated the weighted mean age of the youngest dominant population of zircon analyses, excluding results that were >10% normally or >5% reversely discordant.

The detrital zircon dating was conducted at the University of Texas at Austin in the UT Chron LA-ICP-MS laboratory on a PhotonMachine Analyte G.2 excimer laser with a large-volume Helex sample cell and a Thermo Element2 ICP-MS. Grains were randomly mounted onto double-sided tape, mounted in

epoxy, and polished at UNR. Cathodoluminescence (CL) images of the mounts were collected to guide laser spot analyses. The primary standard used was GJ1 (Jackson et al., 2004) and secondary standards include 91500 (238U/206Pb age of 1065 Ma), and Plesovice (238U/206Pb age of 337 Ma). For analysis of the detrital zircon spectra, I used analyses that were <30% normally or <5% reversely discordant.

**U-Pb Zircon Geochronology Results**

Five samples were dated via U-Pb zircon geochronology (Fig. 15). Sample WJ 11-20-22-01 is a gneiss collected from east of Sheep Creek (Fig. 5). Analysis of 58 grains from this sample yielded a linear array of discordant analyses with an upper intercept of ca. 1.7 Ga and a lower intercept of 131 ± 8 Ma. The upper intercept is interpreted as the Proterozoic protolith age for this sample, with a younger metamorphic event around 131 Ma. A single zircon in this sample gives an age of 147 ± 2 Ma (Fig. 15).

Sample WJ 3-16-22-02 is from a monzonite south of the Mule Spring fault (Fig. 5). A total of 48 grains were analyzed, which yielded concordant ages spanning 201.2 Ma to 170.7 Ma. The weighted mean age of the dominant population of 40 analyses was 191 ± 1 Ma (MSWD = 13), which I interpret as the crystallization age of the monzonite unit (Fig. 15).

Sample AV1 is from the granodiorite complex on the east side of the range (Fig. 5). A total of 38 grains were analyzed, which yielded concordant ages spanning 178.1 Ma to 187.6 Ma. The weighted mean age of the dominant

population of 38 analyses was 183 ± 1 Ma (MSWD = 3.8), which I interpret as the crystallization age of the Avawatz granodiorite complex (Fig. 15).

Sample WJ 11-22-22-05 is from an isolated granitic body in the northeast corner of the map area (Fig. 5). A total of 45 grains were analyzed, which yield concordant ages spanning 138.7 Ma to 157.2 Ma. The weighted mean of 149 ± 1 Ma was determined using all 45 grains analyzed. Some grains had a discordance >10% but were included in the weighted mean because errors on these analyses intersects the concordia line (Fig. 15).

Sample WJ 11-13-21-02 is from a granitic body north of the Mule Spring fault (Fig. 5). Due to issues extracting zircons from the vial at the lab, only eight grains from this sample were analyze yielding concordant ages spanning 101.6 Ma to 104.5 Ma. A weighted mean age of 103 ± 1 Ma was determined from four grains in this sample (Fig. 15). This is interpreted as a likely crystallization age despite the small number of analyses. A single zircon grain from this sample records an age of ~1.79 Ga and is likely a grain that was plucked from the adjacent basement gneiss during the emplacement of this granitic body.

Two samples were analyzed for detrital zircon geochronology (Fig. 16). First, I analyzed a sample of vertically bedded quartzite from the northern flank of the Avawatz Mountains. This unit was previously mapped as the Mesoproterozoic Crystal Springs Formation. Fifty-eight analyses yielded 46 concordant ages spanning ca. 2.5 Ga to 62 Ma, with a dominant population of ages at ca. 1.75 Ga. Analysis of the young age population had Th/U ratios generally <0.1, and I interpret that many of these dates are Late Cretaceous

metamorphic ages overprinting older Proterozoic-Archean detrital zircon ages (Fig. 16A). Lima et al. (2018) documented similar Late Cretaceous thermal overprinting of gneiss samples in Death Valley to the north. The remaining concordant dates are interpreted to comprise the detrital zircons from this sedimentary sample, which a prominent ca. 1.75 Ga age population (Fig. 16A). This distribution is similar to other published detrital zircon spectra for the Crystal Springs Formation.

The Crystal Springs sample was compared to a basement orthogneiss previously sampled by A. V. Zuza from the Death Valley region. Fifty-three spot analyses from the gneiss sample yielded 41 concordant analyses spanning ca. 1.75 Ga to ca. 64 Ma (Fig. 16B). The Late Cretaceous ages likely represent thermal overprinting of ca. 1.75 Ga gneiss. The two detrital zircons datasets suggest that local basement gneiss could have been the source for the Mesoproterozoic Crystal Springs Formation, and both were impacted by a high-temperature overprint in the Late Cretaceous (e.g., Lima et al., 2018) (Fig. 16C).

## DISCUSSION

### Interpretation of field observations

Field mapping has confirmed a change in fault kinematics from the western Avawatz to the eastern range front. In the west, faults associated with the Garlock fault are primarily west-striking subvertical left-slip faults (Fig. 10A). The Mule Spring fault appears to have the most significant geologic offsets because it juxtaposed the Jurassic Avawatz granodiorite against conglomerates

of the Neogene Military Canyon Formation (Fig. 5). This fault does not appear to cut Quaternary deposits, suggesting it may not currently be the most active strand of the Garlock fault (Fig. 5). To the south, the Leach Lake fault is observed to have multiple Quaternary scarps, suggesting it has experienced multiple Quaternary surface ruptures (Fig. 5). This fault does not appear to have large magnitude geologic offsets because the monzonite of Cave Spring and a large Paleozoic pendant of carbonates are found on either side of the fault (Fig. 5).

Faults within the SDVF enter the field area as northwest-striking subvertical right-slip faults (Fig. 5). This study did not attempt to determine the age or amount of slip along these faults. Previous K-Ar ages of the Noble Hills assemblage gives an age of 11.3 Ma (Brady, 1986). However, these ages would need to be confirmed with modern Ar/Ar dating to accurately constrain the age of these units. The Noble Hills assemblage has previously been correlated to similar units in the Owlshead Mountains to the northwest (Brady, 1986). Slip along the SDVF is assumed to have initiated after the deposition of these units. Several of these fault traces cut intermediate Quaternary surfaces, suggesting they can produce Quaternary surface-rupturing earthquakes (Fig. 5).

Detrital zircons collected from the Crystal Spring formation near Sheep Creek and U-Pb ages of zircons from the Proterozoic gneiss both show a Cretaceous age overprint (Fig 15, Fig 16). This could be the result of the emplacement of the Cretaceous granite or an associated intrusion. A thermal event of this age is not observed elsewhere in the Avawatz Mountains south of the Mule Spring fault (Fig. 5). This suggests rocks northeast of the Mule Spring

fault have been transported a significant distance along the SDVF. This is consistent with previous authors who have suggested 40 km of slip has been accommodated on the SDVF (Pavlis and Trullenque, 2021)

Near the intersection of the SDVF and the Mule Spring branch of the Garlock fault, the faults associated the SDVF appear bend to the east (Fig. 5). This deflection could be the result of continued left-slip along the Garlock fault dragging the trace of these faults to the east. Near this intersection the Mule Spring fault beings to display stronger dip-slip kinematics, suggesting it may be starting to transition into a reverse fault (Fig. 5, Fig. 10). Several strands of the SDVF continue to the southwest. The presence of Neogene sediments interpreted to be related to the Noble Hills assemblage on the eastern range front suggests the SDVF once extended further to the southeast, allowing for these units to be offset to their current location (Fig. 5). Field mapping did not find evidence of active strike-slip motion along the eastern trace of the Mule Spring fault. Exposures of the fault along the eastern range front have strong evidence for dip-slip kinematics (Fig 7). The presence of a Quaternary scarp north of Mormon Spring suggests reverse-motion along this fault is still active and represents the most recent phase of deformation in this area (Fig. 5).

The mapped blind thrust deflecting the Quaternary fans along the eastern range front of the Avawatz suggests there may be an additional west-dipping reverse-fault besides the Mule Spring fault (Fig. 5). This fault could represent the propagation of an east directed thrust.

**Interpretation of low-temperature thermochronology data**

Cooling ages provided by zircon He thermochronology are consistent with a Neogene exhumation event rapidly cooling over ~1km of the Jurassic Avawatz granodiorite. The two oldest samples roughly correlate with the highest elevation samples. These samples are interpreted to have been at temperatures below the zircon He closure temperature prior to Neogene exhumation (Fig. 14). The remaining eight youngest samples all cooled through the zircon He closure temperature between 17.2 ± 2.2 Ma and 12.3 ± 3.1 Ma (Fig. 11, Fig. 13). The mean age of these youngest eight samples is 14.7 Ma, which suggests a phase of rapid exhumation of >1 km of rock at ca. 15 Ma. The presence of older ages in the highest structural levels in the Avawatz Mountains with an abrupt transition to younger ages ranging from ~17-12 Ma in lower structural levels indicates the transition from older samples that resided within the fossil PRZ to the younger samples that were at temperatures greater than the zircon PRZ.

The apatite He ages over the same traverse (Reinert, 2004; this study) show younger cooling ages (Fig. 12, Fig. 13, Fig. 14) spanning 4.8 Ma to 7.2 Ma. These data suggest rapid exhumation of >1km at ca. 5–7 Ma.

To test whether the ca. 15 Ma zircon He cooling and ca. 5 Ma apatite cooling represent two pulsed phases of deformation or a single continuous phase of protracted cooling, I ran a series of time-temperature inversions of the data using the HeFTy v2.1.4 modelling software (Ketcham, 2005).

HeFTy allows for the inverse modeling of thermochronology data by inputting parameters like the cooling age of the sample; the measured U, Th, Sm,

and He concentrations; and the size of the grain (Ketcham, 2005). Additional time/temperature data (e.g., crystallization age; unconformities) can be used to constrain the inverse thermal models when available. Inverse modeling with HeFTy randomly generates thermal histories or 'cooling pathways' and selects the pathways that are statistically acceptable and statistically good fits for the input data.

For this study I ran HeFTy inverse models of 2 samples with zircon and apatite He cooling ages. I input the uncorrected He age for each sample; U, Th, Sm, and He concentrations; and the grain size for each analyses. The only constraints I placed on the model were initial starting conditions at a temperature greater than 500°C prior to 180 Ma. These starting conditions were based on U-Pb crystallization ages of the Jurassic Avawatz granodiorite complex. These models were made using HeFTy v2.1.4 to generate 10,000 random cooling paths for each sample.

Inverse modeling of sample WJ 11-13-21-04 used zircon He ages of 17.1 Ma, 15.9 Ma, and 15.4 Ma, with apatite He ages of 5.2 Ma and 3.7 Ma. HeFTy inverse modeling indicates this sample cooled at a relatively constant rate until ca. 35 Ma when this sample started to experience an increased cooling rate (Fig. 17A). However, this break in slope is not constrained by these zircon He and apatite He ages because it occurs at temperatures greater than the closure temperature for these dating methods. The break in slope is essentially random without higher temperature age constraints. The increased cooling rate is

interpreted to be the initiation of exhumation of this sample. This model is consistent with relatively fast and steady cooling below 200°C since ~20 Ma.

Inverse modeling of sample WJ 1-11-22-06 used zircon He ages of 14.7 Ma and 14.9 Ma with apatite He ages of 8.2 Ma, 7.2 Ma, and 6.2 Ma. HeFTy inverse modeling indicates this sample cooled slowly until ca. 20 Ma when this sample began to rapidly cool (Fig. 17B). Inverse modeling of this sample is consistent with relatively fast and steady cooling below 200°C since ~20 Ma.

HeFTy inverse modeling is inconclusive for determining if the younger ca. 6 Ma cooling event is a continuation of the initial ca. 20 Ma event, or a distinct separate event.

A study in the northern Avawatz Mountains produced four mean AHe ages ranging from 2.8 Ma to 5.5 Ma (Chinn, 2013). AFT ages from this study have a large spread with four ages around 10 Ma, two ages between 16-18 Ma, and four ages ranging from 42.9 Ma to 72.2 Ma (Chinn, 2013). The young AHe ages are in the footwall and the hanging wall of the Mule Spring fault in the northern Avawatz Mountains suggesting recent vertical motion along this strand of the Mule Spring fault (Chinn, 2013). The old AFT ages are along the northern rangefront of the Avawatz Mountains in the footwall of the Mule Spring fault, while the younger ages are inboard of the main traces of the Mule Spring fault and other mapped structures (Chinn, 2013). This juxtaposition of AFT ages could have resulted from either dip-slip motion along a strand of the Mule Spring fault, or right-slip motion along faults associated with the SDVF (Chinn, 2013). Forward and inverse modeling of these ages by Chinn (2013) found an increase in cooling

rate from ~3°C/Ma to ~6°C/Ma between 11-9 Ma. These cooling rates would translate to exhumation rates of 0.1 km/Ma to 0.2 km/Ma respectively.

The cooling ages recorded by zircon He and apatite He datasets could have resulted from either punctuated cooling events from 20-12 Ma and 5 Ma or by steady, progressive cooling starting ca. 20 Ma. There are several possibilities for the drivers of these cooling events. One possibility is that thrust-related hanging wall uplift and coupled erosion could have exhumed the thermochronology samples (e.g., Zheng et al,.2006). Alternatively, normal faulting could have exhumed the footwall rocks during progressive hanging wall removal and footwall rebound (e.g.,Lee et al., 2009; Bidgoli et al., 2015). Lastly, complex strike-slip-related transpressional deformation could have popped up the range, with coupled erosion, to cool the thermochronology samples (e.g. Giorgis et al., 2017).

Both zircon He and apatite He datasets from the eastern range front show a general trend of increased sample age with increased elevation and distance from the mapped trace of the Mule Spring fault. This pattern is consistent with exhumation being driven by east-directed thrusting along the Mule Spring fault or a related structure. If the exhumation of the Avawatz Mountains was caused by motion along the Arrastre Spring fault on the southwest side of the range, then cooling ages would be expected to young to the west. However, the opposite trend is seen in these data.

If the exhumation of these samples is the result of thrust faulting along the Mule Spring fault, the cooling of the samples is achieved through the erosion of

the overlying rocks. The amount of material that must be removed is dictated by the depth of the samples when exhumation occurred. This depth could vary based on the geothermal gradient at the time exhumation started. Similar studies in the region have assumed a geothermal gradient of 25-30°C/km (Holm and Dokka, 1991; Bidgoli et al., 2015: Additional citations). If the geothermal gradient was 30 °C/km, the approximate depth of the zircon PRZ (130°C-200°C) is 4.3 km to 6.7 km. The structurally deepest samples were exhumed from ~1km below the interpreted zircon PRZ. Therefore, at least 5-8 km of erosion is required since ca. 20 Ma. to exhume these samples from below the zircon PRZ to the Earth's surface. This would translate to exhumation rates of 0.25km/Ma to 0.4 km/Ma respectively. These are slightly higher than the younger exhumation rate of 0.2 km/Ma proposed by Chinn (2013).

Sediments sourced from the unroofing of the Avawatz would have been deposited in nearby Neogene basins. Blocks of Precambrian rocks and Paleozoic carbonates in landslide deposits of the Noble Hills assemblage have been interpreted to have been sourced from an unroofing event of the Avawatz. It is possible the ca. 20-15 Ma exhumation event recorded in the zircon He thermochronology is responsible for the initial unroofing of the Avawatz, causing erosion of the Precambrian and Paleozoic cover.

**Regional tectonic implications**

Field observations from the Avawatz Mountains indicate the western portion of the range is dominated by strike-slip deformation. The SDVF enters the

study area as a series of parallel northwest-striking right-slip faults. Where observed, these faults tend to have strike-slip kinematic indicators. The Garlock fault enters the study area as two subparallel west-striking left-slip faults. West of the intersection with the SDVF, faults associated with the Garlock fault are west-striking subvertical faults with strike-slip kinematics (Fig. 5, Fig. 10A). At the intersection of the SDVF and the Garlock fault, the Mule Spring fault appears to deflect and override faults associated with the SDVF (Fig. 5). Near the intersection between the faults, the fault orientations begin to vary (Fig. 10B). At this intersection with the SDVF the Mule Spring fault begins to display a more pronounced dip to the south, as indicated on the geologic map by fault traces “V-ing” up drainages pointing toward the south (Fig. 5). As this fault continues to the east, the west-southwest dip of the fault plane becomes more pronounced. At the head of Anvil Canyon, the trace of the Mule Spring fault has a large “V” up the canyon, indicating the fault plane is dipping to the southwest (Fig. 5). Where exposed along the eastern range front, the Mule Spring fault is expressed as a west-dipping reverse fault placing the Jurassic granodiorite complex over Neogene and Quaternary sediments (Fig. 5, Fig. 9). This fault shows strong evidence for dip-slip kinematics based on down-dip slickenlines (Fig. 9B). These observations suggest a spatial change in fault kinematics from primarily strike-slip motion in the western Avawatz Mountains to primarily dip-slip motion in the eastern Avawatz Mountains. This change in fault kinematics is consistent with east-northeast directed shortening in the Avawatz Mountains.

Low-temperature thermochronology ages record cooling of the structurally lowest portions of the Avawatz Mountains beginning at ca. 20 Ma based on inverse modeling (Fig 17). Zircon He age vs elevation profiles indicate rapid exhumation of over 1 km of rocks through the zircon PRZ from 17-12 Ma, with a mean cooling age of ~15 Ma for the youngest eight samples (Fig. 14). The ~15 Ma phase of cooling is similar in age to estimates for the initiation of left-slip along the Garlock fault to the west (Burbank and Whistler, 1987; Blythe and Longinotti, 2013; Andrew et al., 2014; Sample, 2018) (Fig. 18), and generally older than estimates for the initiation of slip along the SDVF (Holm and Dokka, 1991, 1992; Bidgoli et al., 2015) (Fig. 18). These timing constraints are consistent with initial exhumation of the Avawatz Mountains related to the initiation of left-slip faulting along the Garlock fault. In this case, eastward displacement of the Mojave block on the south side of the Garlock fault led to contractional deformation south of the fault at its eastern terminus (e.g., Zuza and Yin, 2016), which developed into an east-vergent thrust belt as a termination structure of the Garlock fault (Fig. 2C).

Thermochronology data presented here are consistent with ca. 15 Ma exhumation and rapid cooling, which continued to ca. 5 Ma. The apatite He ages may record an accelerated pulse of deformation at ca. 5 Ma, or it may simply track progressive cooling since middle Miocene time. Inverse modeling of thermochronology ages is consistent with a model of continuous exhumation starting ca. 20-15 Ma and continuing until the present. Due to the few constraints in the thermochronology modeling, additional higher temperature

thermochronology ages could be useful in constraining the higher temperature history of these rocks.

That said, the similarity of the apatite He ages to documented cooling ages within the southern Death Valley system may suggest a linkage between the SDFZ and Avawatz Mountains at ca. 5 Ma. In this case, the right-slip SDFZ may have linked with the Avawatz Mountains, ultimately forming a left-stepping right-slip restraining bend that continued to exhume the Avawatz Mountains in a complex transpressional zone since late Miocene time.

The extrusion and transform fault models for the Garlock fault do not predict shortening at the eastern terminus of the fault coeval with left-slip along the fault (Hill and Dibblee, 1953, Davis and Burchfiel 1977) (Fig. 2). These models predict a younger exhumation age of the Avawatz Mountains where exhumation is driven primarily due to contractional deformation from a restraining bend in the SDVF (Fig. 4B). The rotating fault model predicts shortening at the eastern tip of the Garlock fault resulting from clockwise rotation of the Mojave (Fig. 2C). This shortening would be northeast- to east-vergent thrusting, similar to what is observed in the Avawatz. This model also predicts shortening to be coeval with the initiation of left-slip along the Garlock fault. Low-temperature thermochronology ages from the Avawatz Mountains suggest the range started to experience exhumation ca. 15 Ma, similar to estimates for the initiation of left-slip along the Garlock fault (Burbank and Whistler, 1987; Blythe and Longinotti, 2013; Andrew et al., 2014; Sample, 2018) (Fig. 18).

An alternative possibility is that the cooling recorded in the Avawatz Mountains could be caused by tectonic exhumation of the hanging wall in a normal fault. This explanation requires lower magnitudes of exhumation since the rocks are being tectonically exhumed rather than requiring additional erosion to exhume the rocks to the surface. The only mapped extensional structure in the Avawatz Mountains is the Arrastre Spring fault on the southwest side of the range (Spencer, 1981; Brady, 1986) (Fig. 5). Traces of this fault are concealed beneath the Arrastre Spring Formation, suggesting it has not been active since at least 11 Ma (Spencer, 1981; Brady, 1986). This makes it difficult to explain the continued exhumation until at least 6 Ma recorded in the apatite He ages. Extensional events of a similar age have been proposed north of the Garlock fault to the west in the Tehachapi Mountains and along the Sierra Nevada frontal fault system (Blythe and Longinotti, 2013; Lee et al., 2023).

A younger phase of deformation related to slip along the SDVF could be overprinting the older phase of deformation associated with the Garlock fault, resulting in continued and active deformation of Quaternary units. Hatem and Dolan (2018) argue that since the establishment of significant dextral shear in the Eastern California Shear Zone at ca. 3 Ma, there has been enough rotation of the Garlock fault to explain the ~1 mm/yr Quaternary slip rate along the eastern portion of the fault. This continued rotation of the fault could be driving continued east-northeast-directed shortening as the northeast Mojave rotates clockwise. The displacement of Quaternary fan surfaces indicates Quaternary slip along the eastern rangefront trace of the Mule Spring fault.

## CONCLUSIONS

Field observations and new detailed geologic mapping reveal an along-strike change in fault kinematics from west to east within the Avawatz Mountains. The western portion of the range is dominated by strike-slip faults, while the eastern side of the range is characterized by west-dipping reverse faults. This change in fault kinematics is consistent with an eastward transition from left-slip to east-directed shortening in the Avawatz Mountains.

Zircon and apatite (U-Th)/He cooling ages indicate that samples from the Avawatz Mountains experienced rapid cooling from ca. 17-15 Ma. The structurally highest samples have cooling ages that are greater than 17 Ma, suggesting that the lower-elevation samples with younger cooling ages resided at temperatures greater than the zircon He PRZ prior to 17-12 Ma. These cooling ages are coeval with estimates for the initiation of left-slip on the Garlock fault (Burbank and Whistler, 1987; Andrew et al., 2014; Sample, 2018). It is possible that this cooling records tectonic exhumation at the eastern terminus of the Garlock fault.

These observations support a rotating fault model with contractional deformation starting in the Avawatz by ca. 15 Ma. This deformation is partially overprinted by transpressional deformation associated with a restraining bend in the right-slip SDVF. Cross-cutting relationships between the fault zones and Quaternary scarps on the eastern range front suggest that some strands of the Garlock fault, such as the Leach Lake fault, are still active.

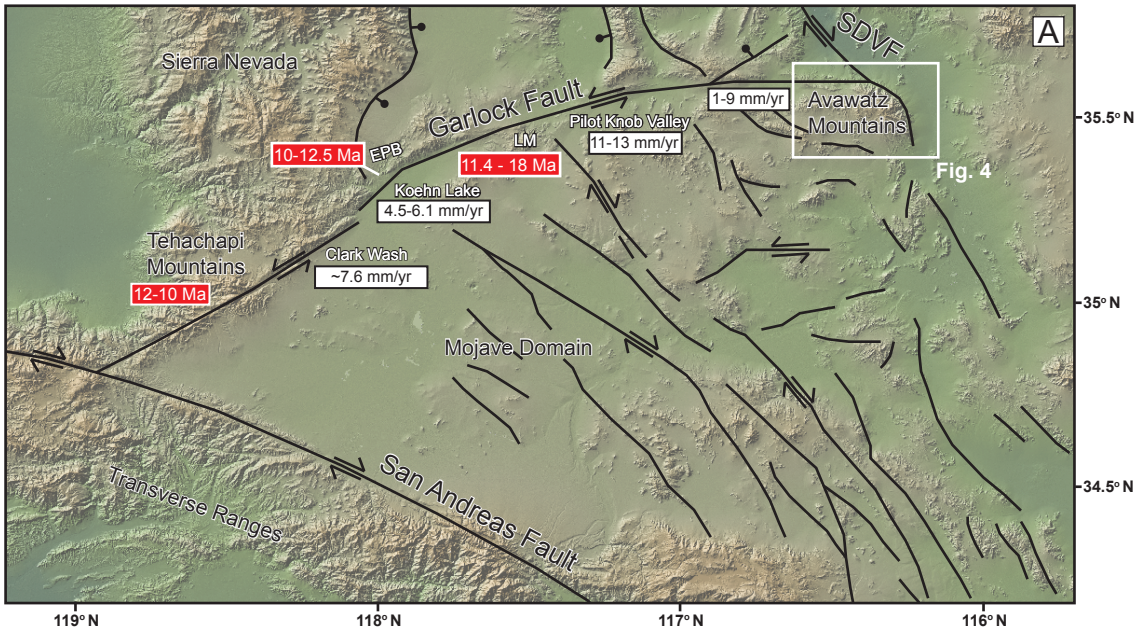


Figure 1. Color-shaded relief map of the greater Mojave region with major faults shown in black. Normal faults are indicated with bar-and-ball on the footwall, major strike-slip faults are indicated by arrows with relative motion. White box shows location of the study area in the Avawatz Mountains at the eastern end of the Garlock fault. Red boxes show published ages for the initiation of the Garlock fault. Data Sources: Tehachapi Mountains- Blythe and Longinotti (2013); El Paso Basin- Burbank and Whistler (1987), Sample (2018); Lava Mountains- (Andrew et al., 2014). White boxes show Quaternary geologic slip rates at sites along the Garlock fault. Data Sources: Clark Wash- McGill et al., (2009); Koehn Lake- Clark and Lajoie (1974); Pilot Knob Valley- Rittase et al., (2014); Leach Lake/Avawatz- McGill and Sieh (1993). EPB – El Paso Basin; LM – Lava Mountain; SDVF – Southern Death Valley fault.

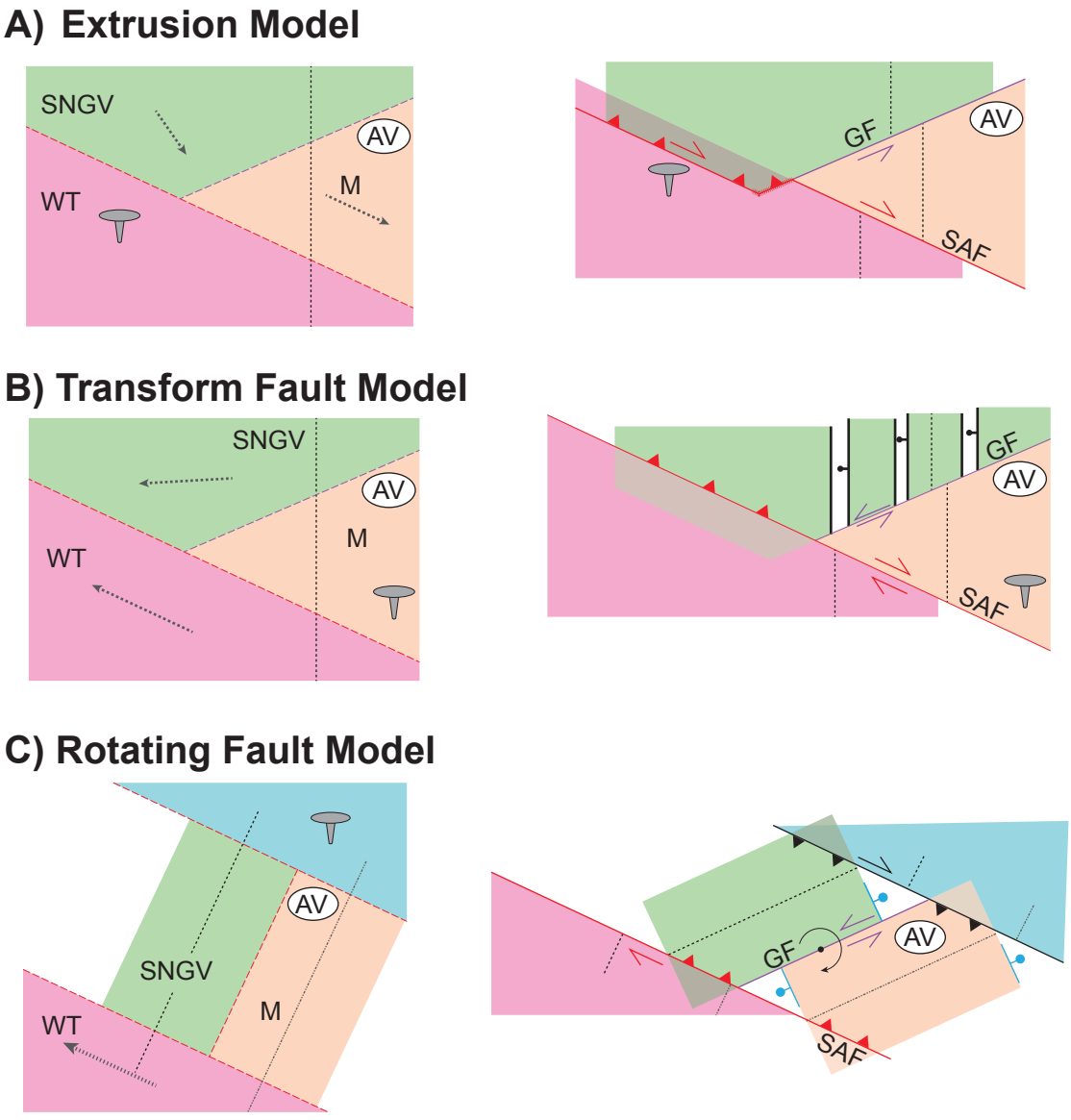


Figure 2. Tectonic models for the evolution of the Garlock fault. See text for more detailed discussion (A) Extrusion model of Hill and Dibblee (1953), eastward extrusion of the Mojave block is driven by conjugate slip on the Garlock and San Andreas faults. (B) Transform fault model where differential extension between the western Basin and Range and the Mojave block drives left-slip on the Garlock fault (Hamilton and Myers, 1966; Davis and Burchfiel, 1973). (C). Rotating fault model where the Garlock fault has rotated clockwise due to right-slip in the Eastern California Shear Zone resulting in contractional deformation in the northeast Mojave block (Garfunkel, 1974; Humphreys and Weldon, 1994; Platt and Becker, 2013).

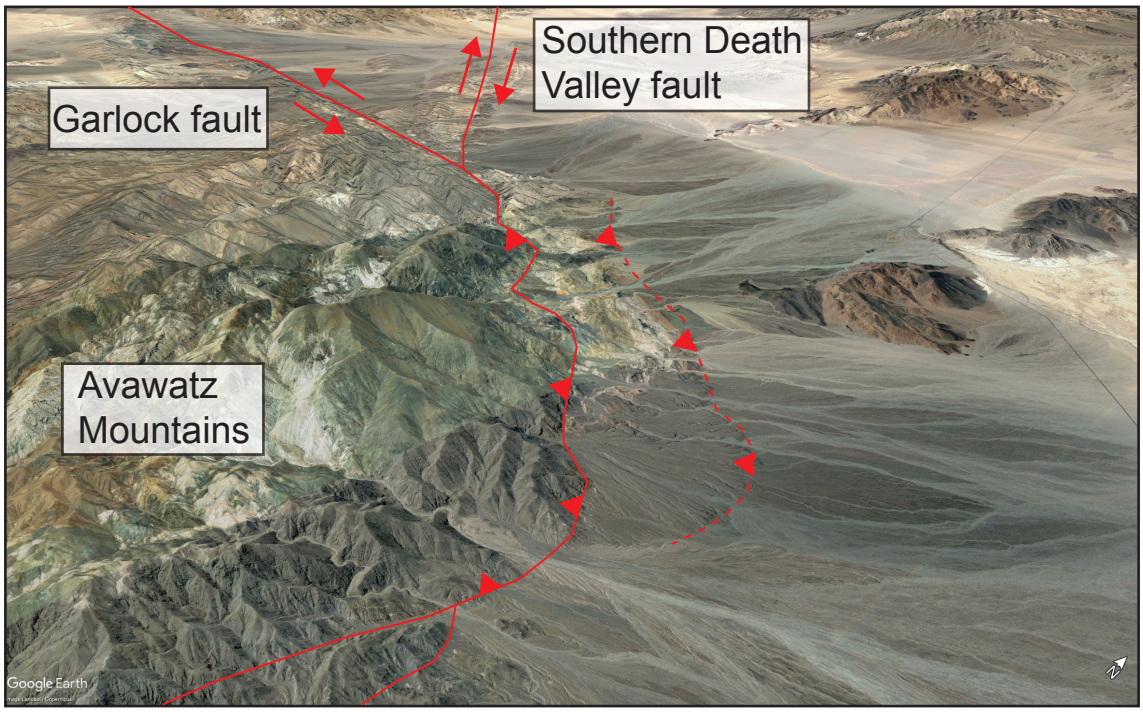


Figure 3. Oblique satellite image from Google Earth of the Avawatz Mountains looking north-west. Traces of the Garlock and Southern Death Valley faults in red. Arrows on faults show relative sense of slip. Triangles are on the hanging wall of reverse faults. Dashed faults are inferred.

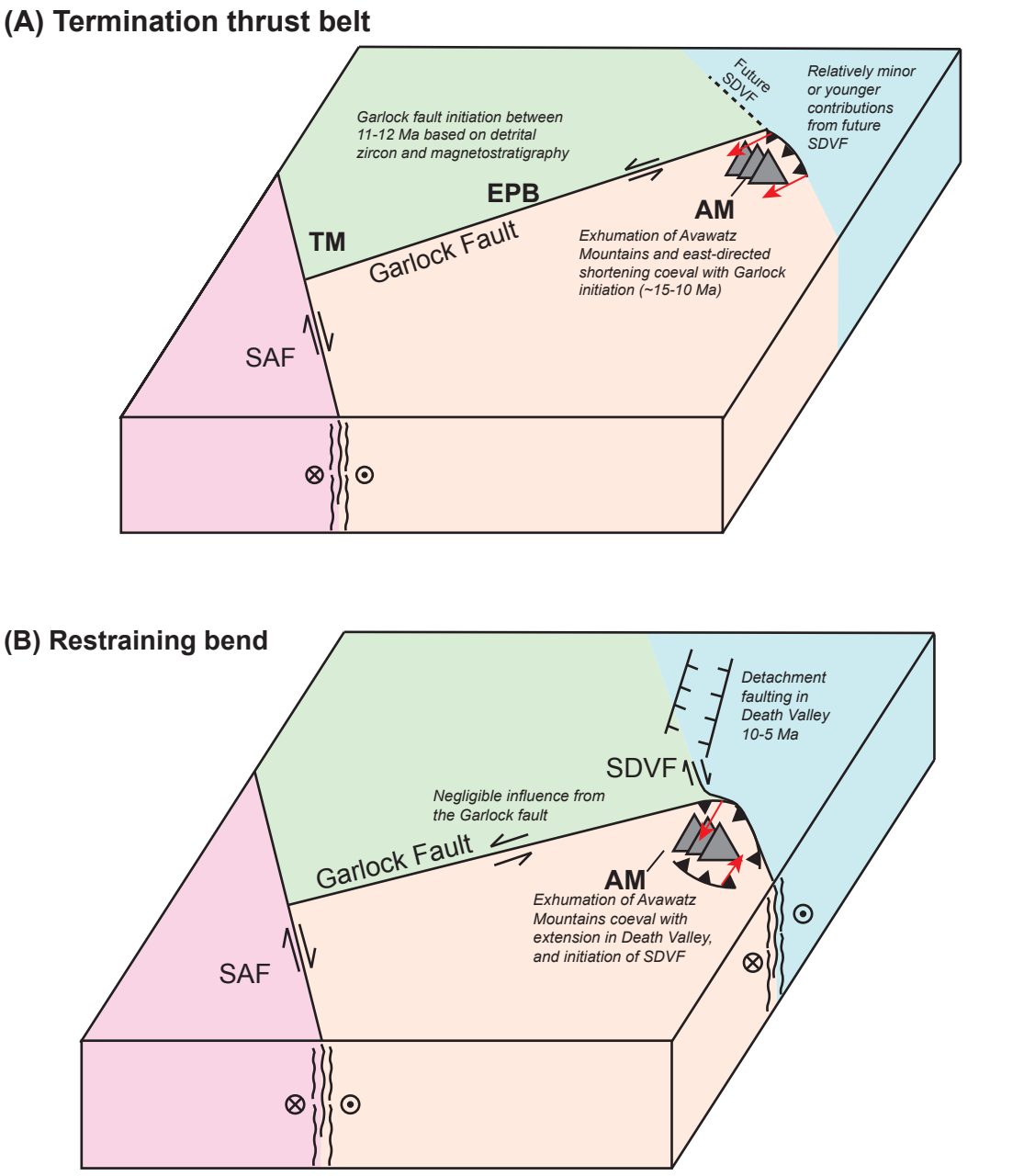


Figure 4. (A) Model for the exhumation of the Avawatz along a termination thrust at the eastern end of the Garlock fault. Left-slip on the Garlock fault is being accommodated as east-directed thrusting. This model predicts (1) primarily west-dipping, reverse faults and east-striking strike-slip fault, (2) exhumation of the Avawats occurring ca. 18-11 Ma, coeval with estimates for the initiation age of the Garlock fault, and (3) rates and magnitudes of shortening recorded in the Avawatz be comparable to estimates along the Garlock fault. Red arrows show expected direction of fault striations. (B) Model for the exhumation of the Avawatz due to a restraining bend in the SDVF. This model predicts (1) Complex restraining bend fault geometries with varying fault orientations and kinematics, (2) exhumation ca. 10-5 Ma coeval or younger than extension in Death Valley, and (3) fault activity dominated by northwest-striking right-slip faults. Red arrows show expected orientations of fault striations.

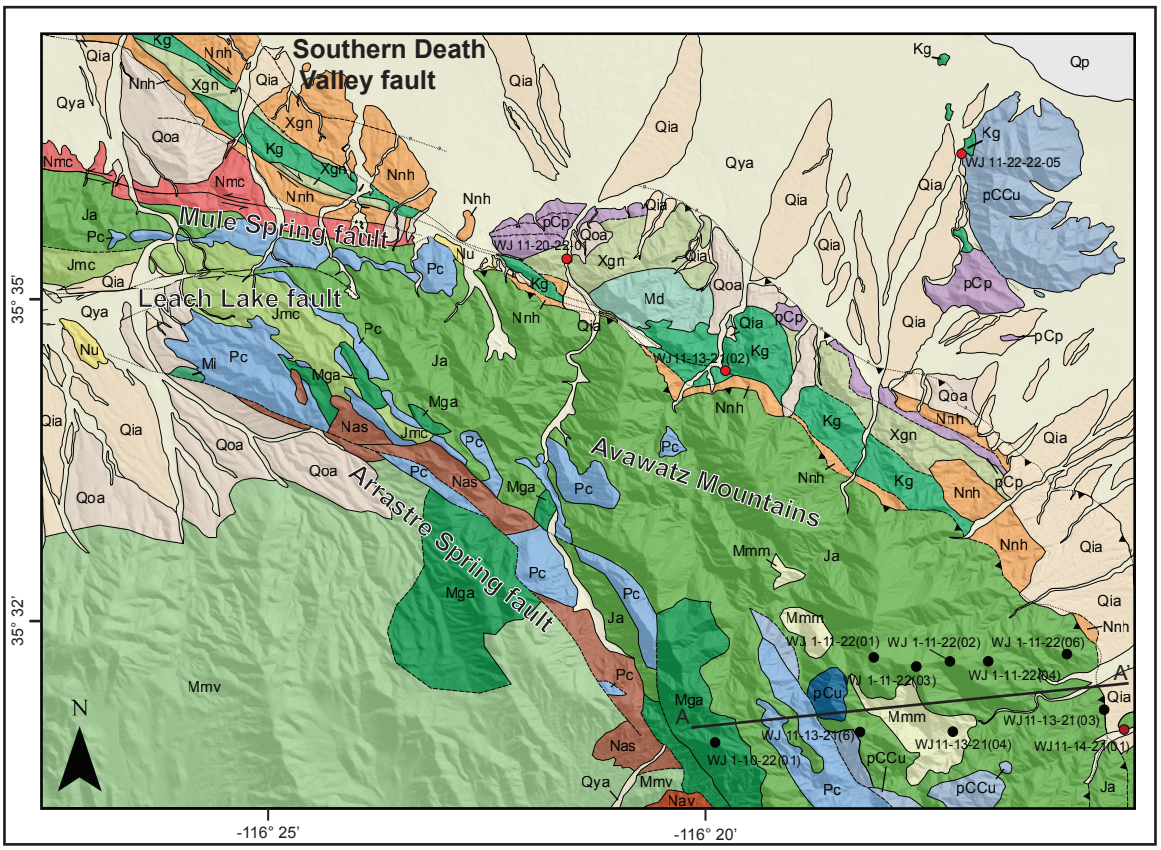


Figure 5. Simplified geologic map of the Avawatz Mountains. Basemap is a 10m DEM with a 45 degree illumination. Zircon U-Pb samples are red circles. Zircon He samples are black circles. Samples with both U-Pb ages and He ages are maroon.

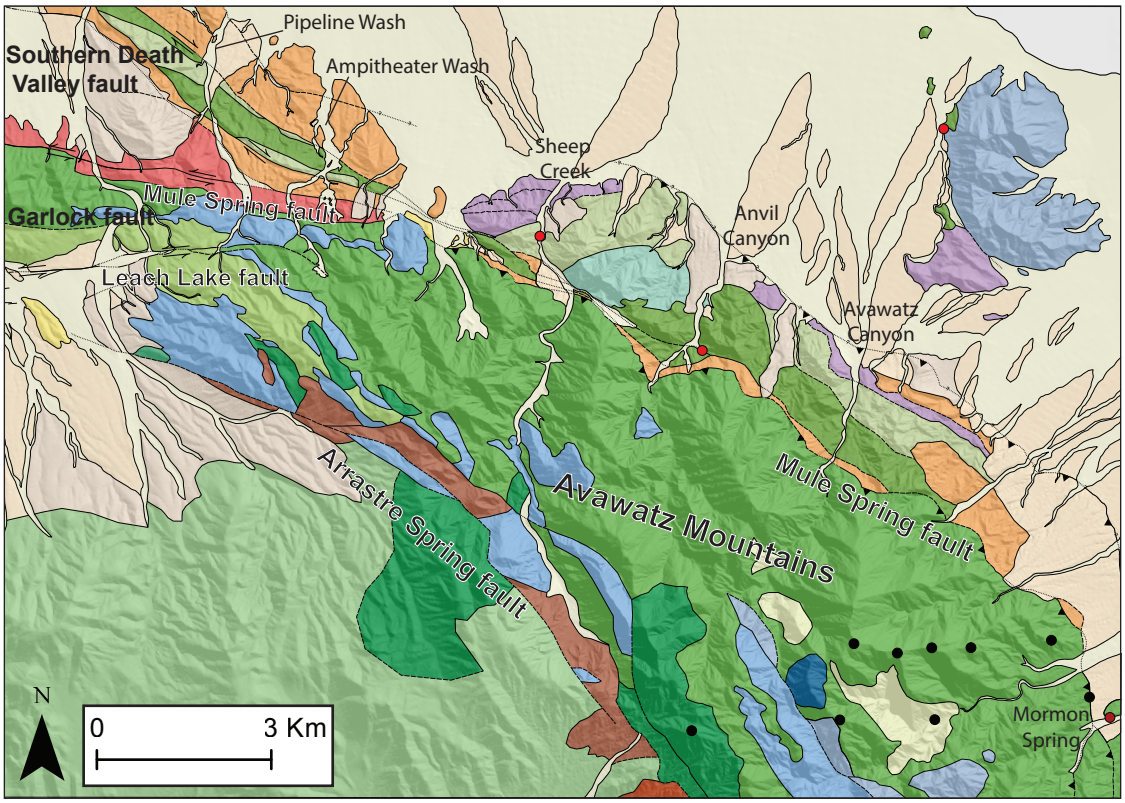


Figure 6. Simplified map of the Avawatz Mountains with location names used in this study. See figure 5 for explanation of map units and symbols.

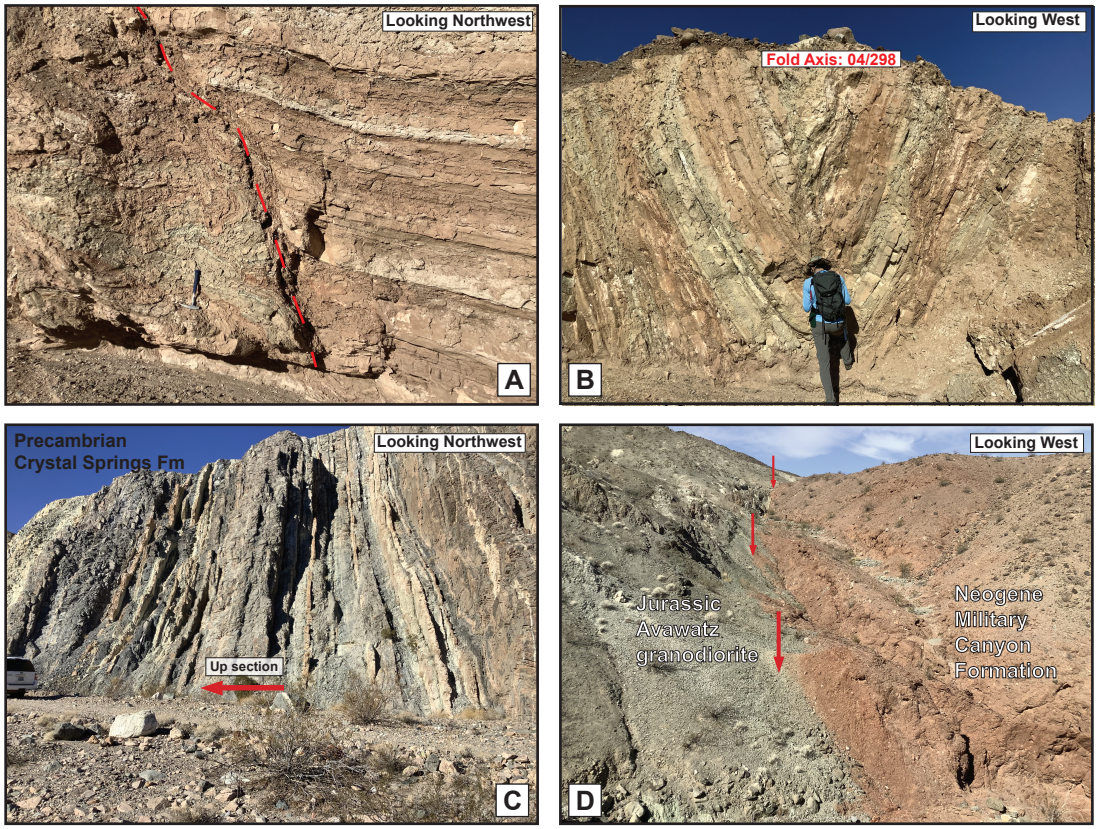


Figure 7. Photos of relevant field relationships from mapping. (A) Faulted bed of the Noble Hills Assemblage in Pipeline Wash (Fig. 5). Red dashed line shows location of secondary fault trace. Notice the highly deformed sedimentary beds near the fault. Hammer for scale. (B) Folded sediments of the Noble Hills Assemblage in Pipeline Wash (Fig. 5). Fold hinge is weakly plunging to the west. Geologist for scale. (C) Beds of the Crystal Spring Formation at the mouth of Sheep Creek (Fig. 5). Red arrow indicates the stratigraphic top of the section. Beds in this location are neat vertical to locally overturned. White rocks outcropping in the upper left of the photo is talc alteration occurring along the margins of a diabase intrusion. Truck for scale. (D) Exposure of the Mule Spring fault juxtaposing the Jurassic Avawatz granodiorite (left) against the Neogene Military Canyon Formation (right). Red arrows point to the trace of the fault. Boulders seen in the closest wash are ~0.5m.

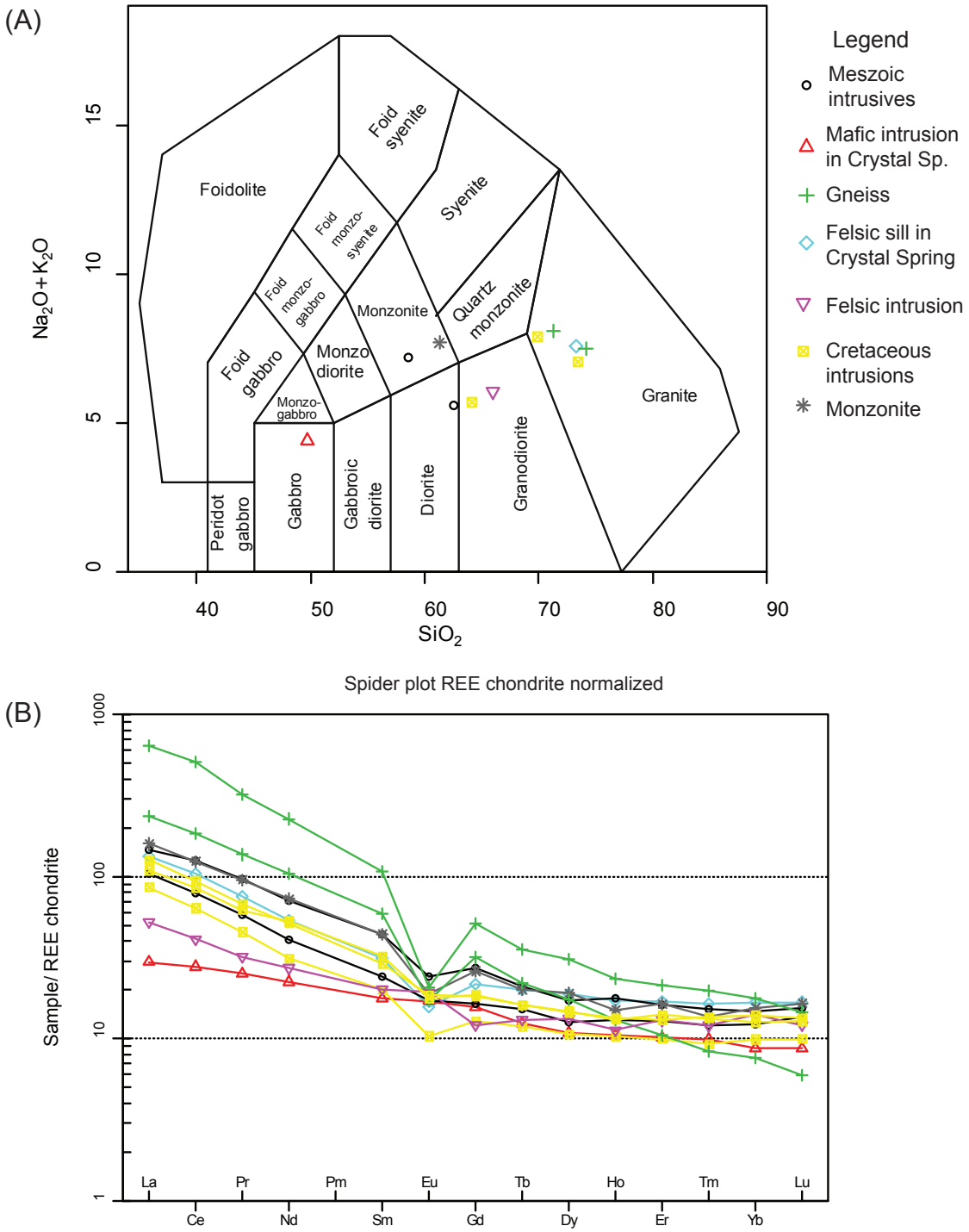


Figure 8. (A) total alkali versus silica plot (Middlemost, 1994) of samples from the Avawatz Mountains. Most intrusive samples plot in the diorite to granite fields. A sample of the mafic intrusion from the Crystal Springs Formation plots as a gabbro. (B) REE chondrite normalized spider plot of geochemical samples (Boynton, 1984). All samples show a negative Eu anomaly indicative of plagioclasese fractionation except for the mafic intrusion in the Crystal Spring Formation. Colors correspond to samples from figure 8A.

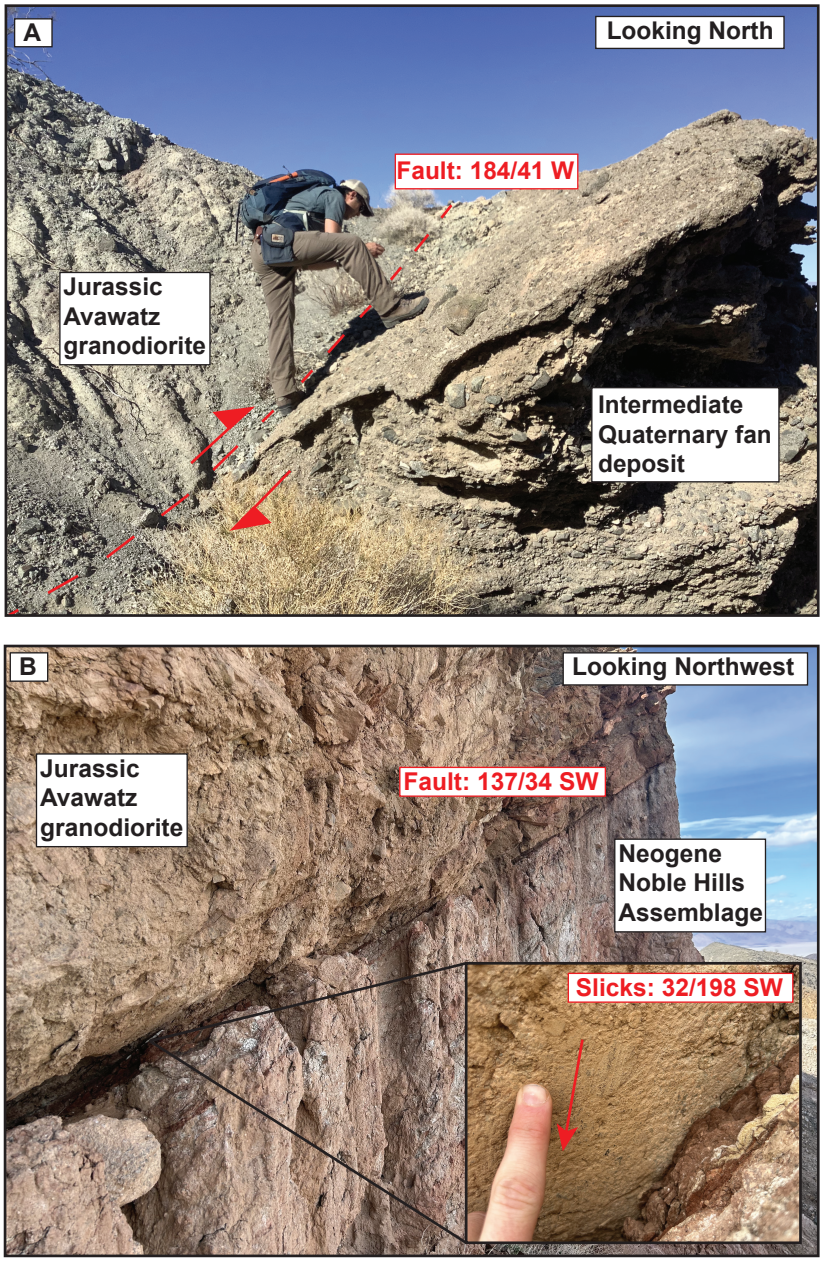


Figure 9. (A) Exposure of the Mule Spring fault north of Mormon Spring (Fig. 5). Fault plane is striking 184 dipping 41 to the west placing Jurassic Avawatz granodiorite over intermediate aged Quaternary fan. Geologist for scale. See map for photo location. (B) Exposure of Mule Spring fault in the northeast map area. Fault plane is striking 137 dipping 34 to the southwest placing Jurassic Avawatz granodiorite over the Neogene Noble Hills assemblage. Slickelines on the fault are shown in the inset image plunging 32 to the southwest. Note the well-developed gauge zone along the fault, indicating a significant amount of slip has occurred along this fault plane.

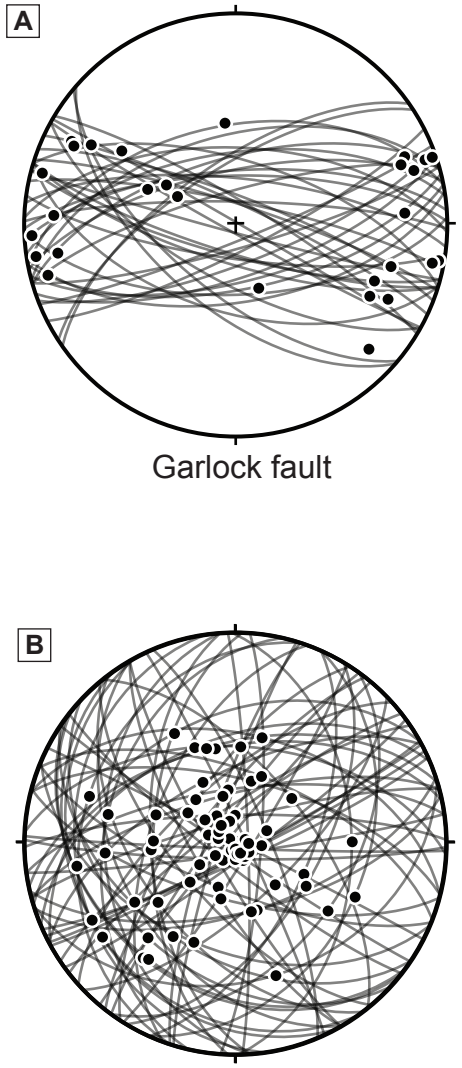


Figure 10. Equal area lower hemisphere stereonets of fault planes and slickenline orientations. Fault planes are shown by grey lines, slickenlines are black circles. (A) Faults and slickenlines from structures related to the Garlock fault. (B) Faults and slickenlines from east of the intersection of the Garlock and SDVF.

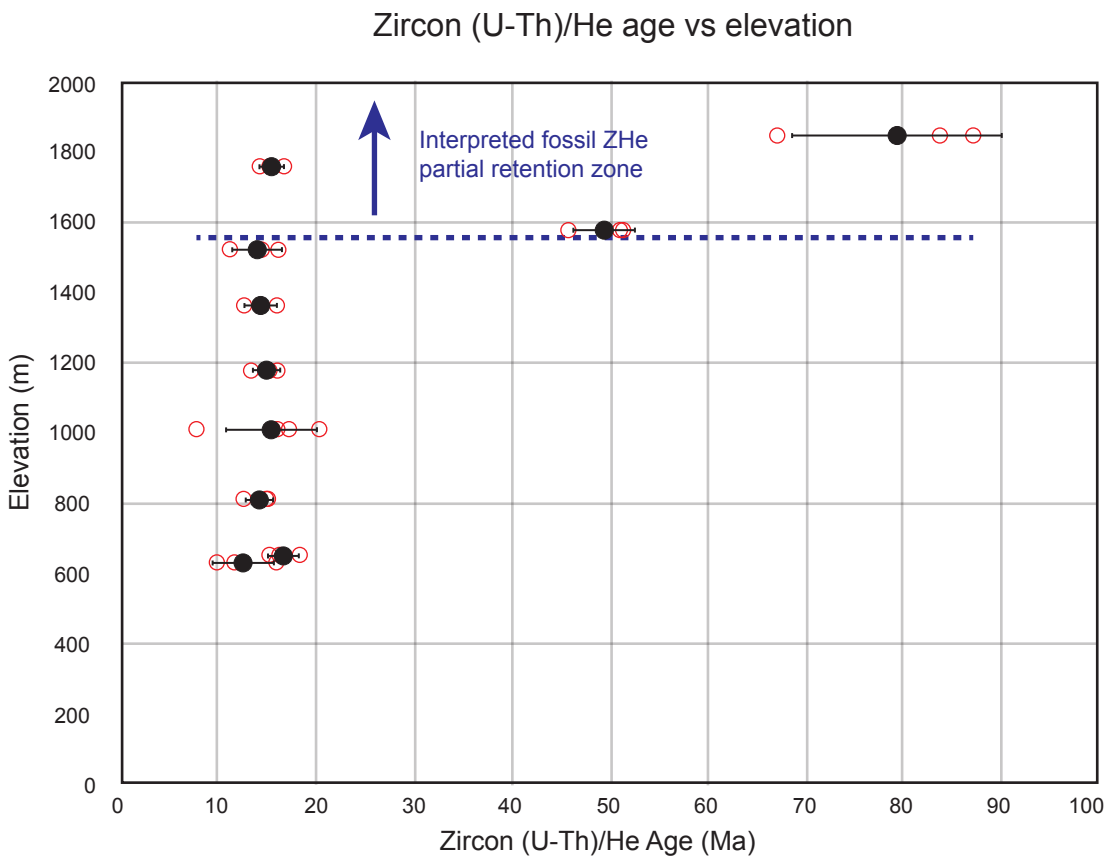


Figure 11. Plot of zircon (U-Th)/He age versus elevation for samples from transect across the eastern trace of the Mule Spring fault. Red open circles are individual zircon ages from each sample. Black closed circles are the mean age for each sample, black bars are 2 sigma errors. Blue dashed line shows the interpreted fossil zircon partial retention zone.

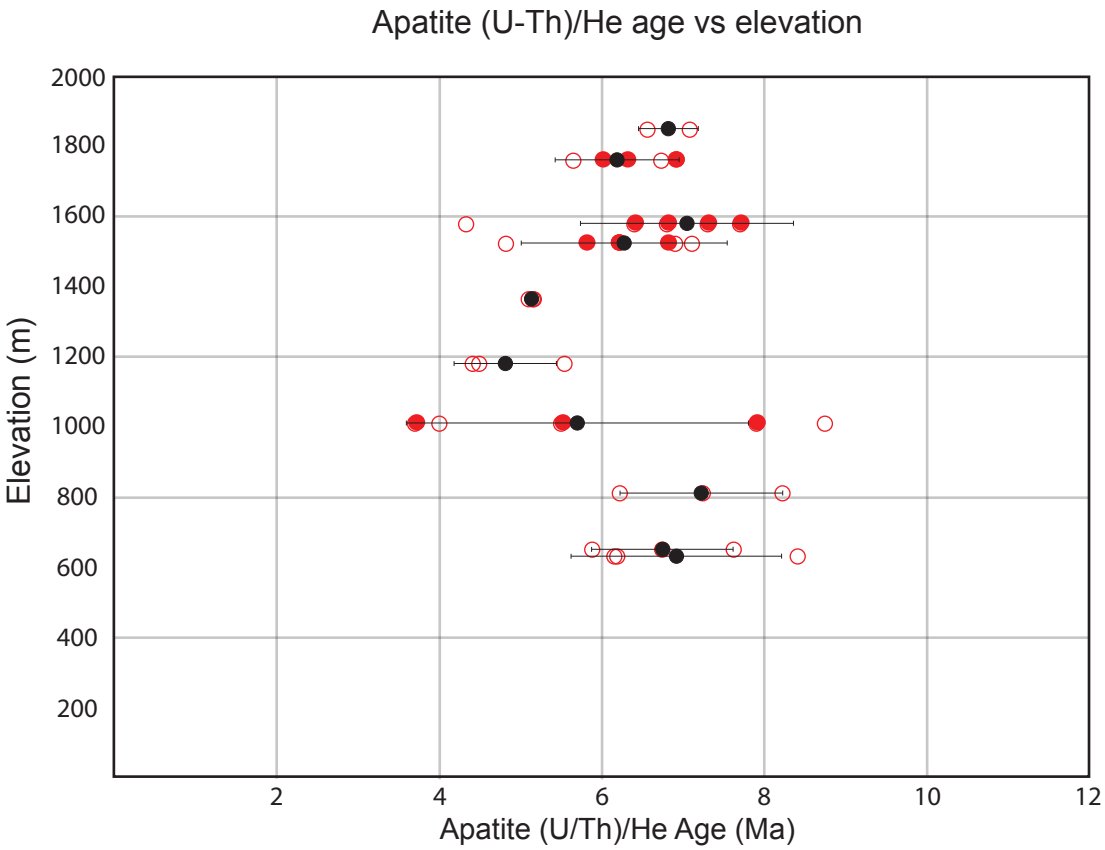


Figure 12. Plot of apatite (U-Th)/He age versus elevation for samples from transect across the eastern trace of the Mule Spring fault. Red open circles are individual apatite ages from Reinert (2004). Red closed circles are individual apatite ages from this study. Black closed circles are the mean age for each sample, black bars are 2 sigma errors.

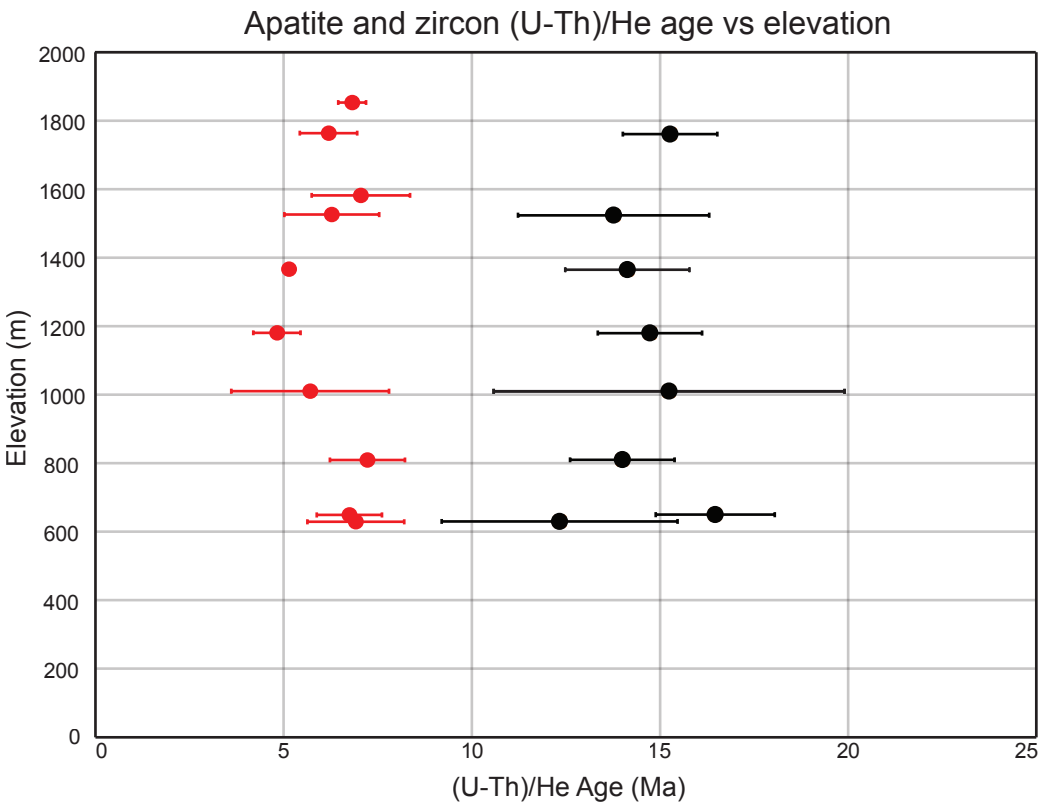


Figure 13. Plot of the mean apatite (U-Th)/He age (red) and mean zircon (U-Th)/He age (black) versus elevation. This plot excludes the two zircon ages that are >25 Ma to focus on the Neogene history. Error bars are 2 sigma errors.

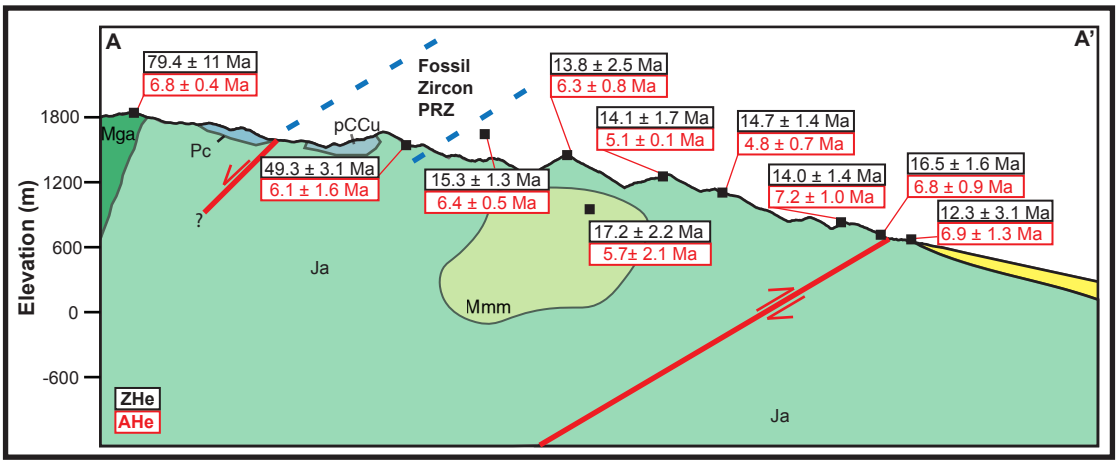


Figure 14. Cross section along line A-A' from figure 5. Low-temperature thermochronology samples are black squares, these locations are projected onto the cross section line. Zircon He cooling ages are shown in boxes outlined in black. Apatite He cooling ages are shown in boxes outlined in red. Errors are 1 sigma error. Blue dashed lines show interpreted location of the zircon partial retention zone. Major faults are in red, with arrows showing relative sense of slip.

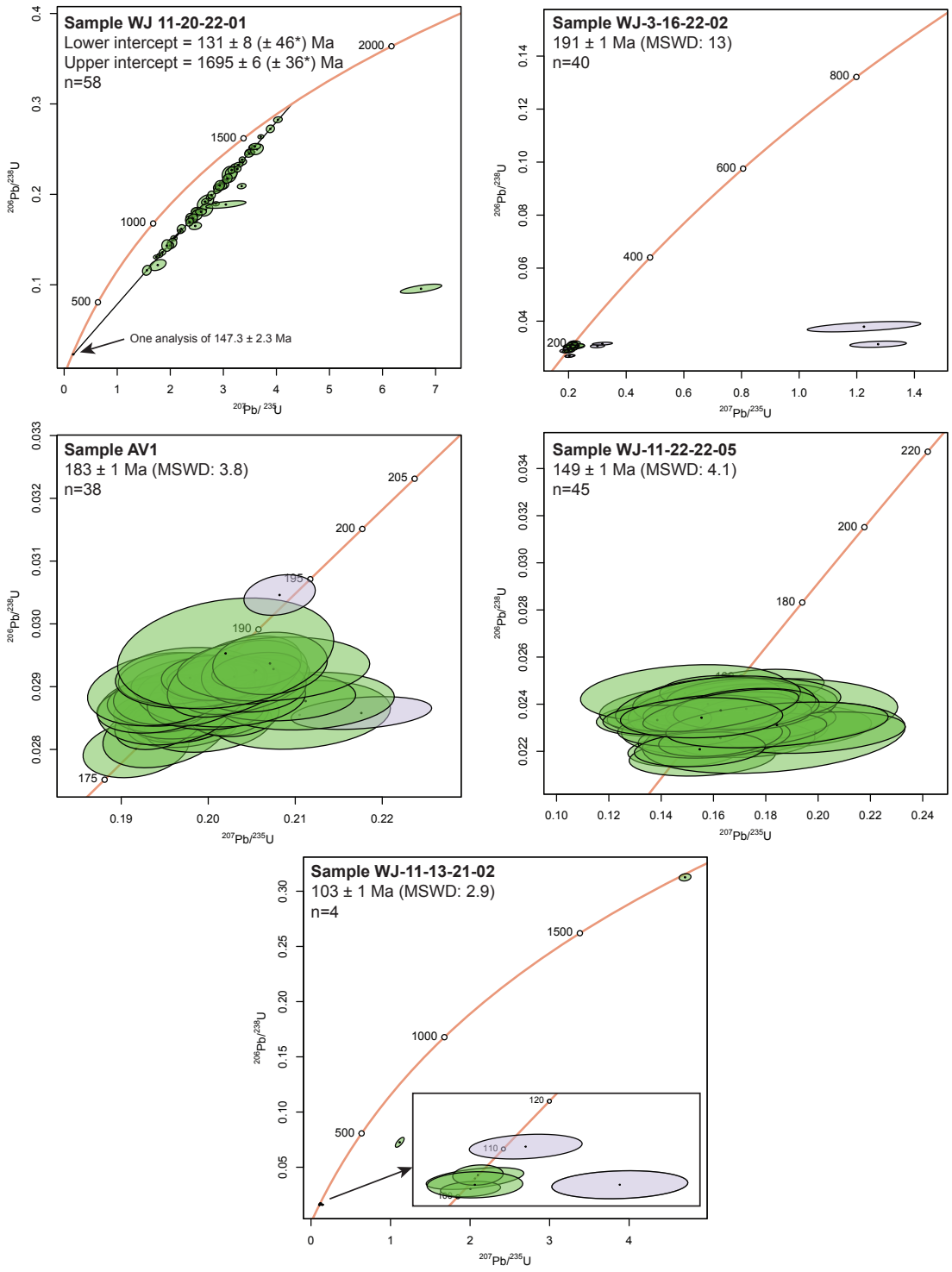


Figure 15. Concordia plots of zircon U/Pb ages with weighted mean age. Green ovals are analyses included in the weighted mean age, purple ovals are excluded from weighted mean. See text for methods. * indicates the analytical uncertainty with overdispersion.

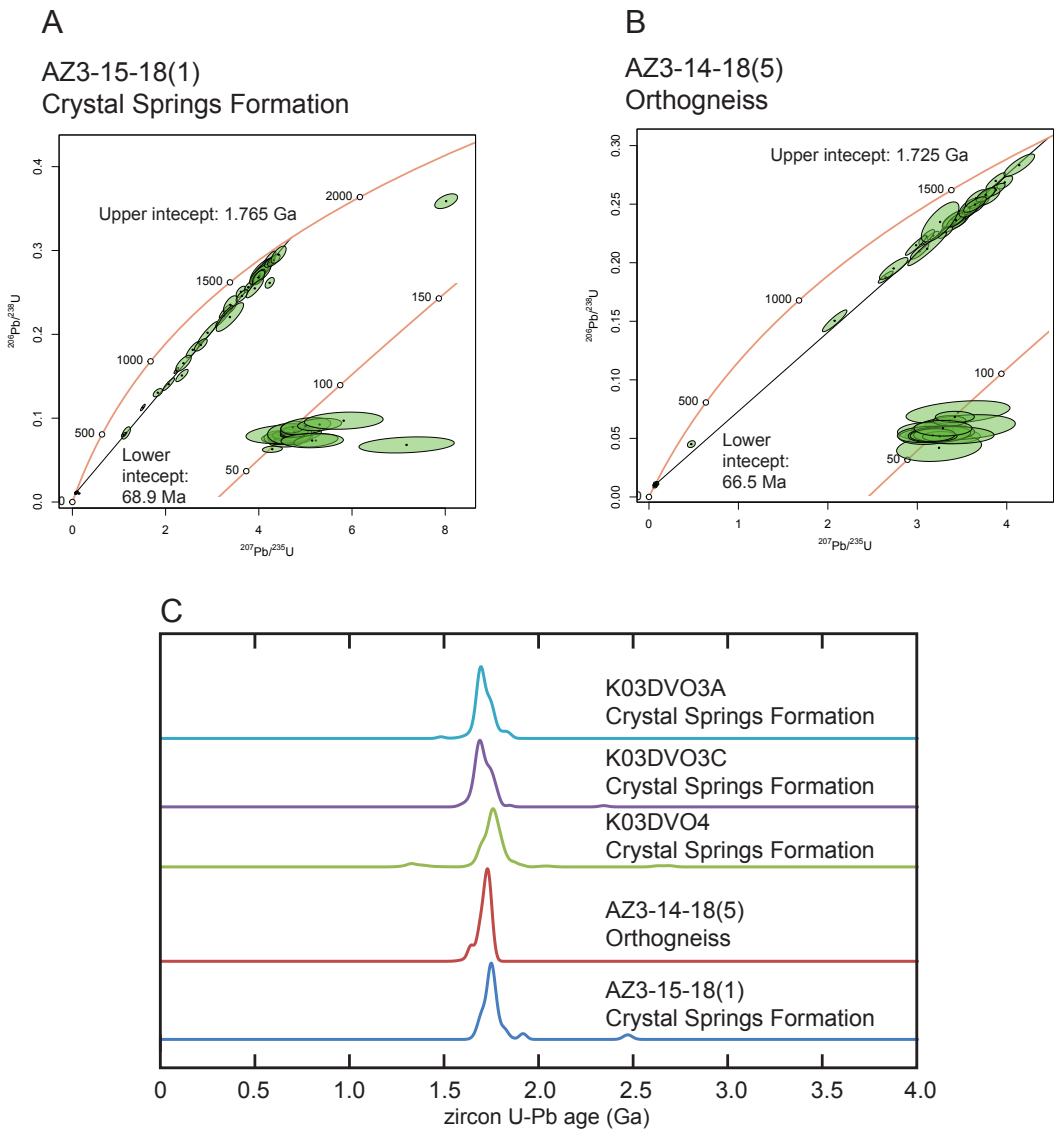


Figure 16. (A) Concordia plot of detrital zircons collected from the Crystal Spring Formation. Upper intercept of 1.8 Ga is interpreted to be the Proterozoic protolith age of the rocks sourcing the zircons for the Crystal Spring Formation. The lower intercept ca. 70 Ma indicates this sample experienced a Cretaceous heating event. A similar event is observed in zircon samples of the basement gneiss is Figure X. (B) Concordia plot of zircons from the orthogneiss north the Mule Spring fault near Sheep Creek (Fig. 5). Upper intercept of 1.7 Ga is interpreted to be the Proterozoic protolith age. The lower intercept of ~67 Ma indicates this sample experienced a Cretaceous heating event, resetting the zircon U-Pb age. (C) Histograms comparing detrital zircon and zircon ages from this study to detrital zircon ages of the Crystal Spring formation from Mahon and others (2014). Sample K03DV03 is from the basal conglomerate of the Crystal Spring Formation in the Kingston Range. Sample K03DV04 is from the lower Crystal Spring Formation in the Kingston Range. The similar peaks of zircon ages ca. 1.7 Ga confirm this unit in the Avawatz Mountains is the Proterozoic Crystal Spring Formation. The samples from south of the Mule Spring fault lack evidence for a Cretaceous heating event, suggesting the Crystal Spring Formation and the Proterozoic gneiss have been transported along the SDVF and juxtaposed against the Avawatz Mountains.

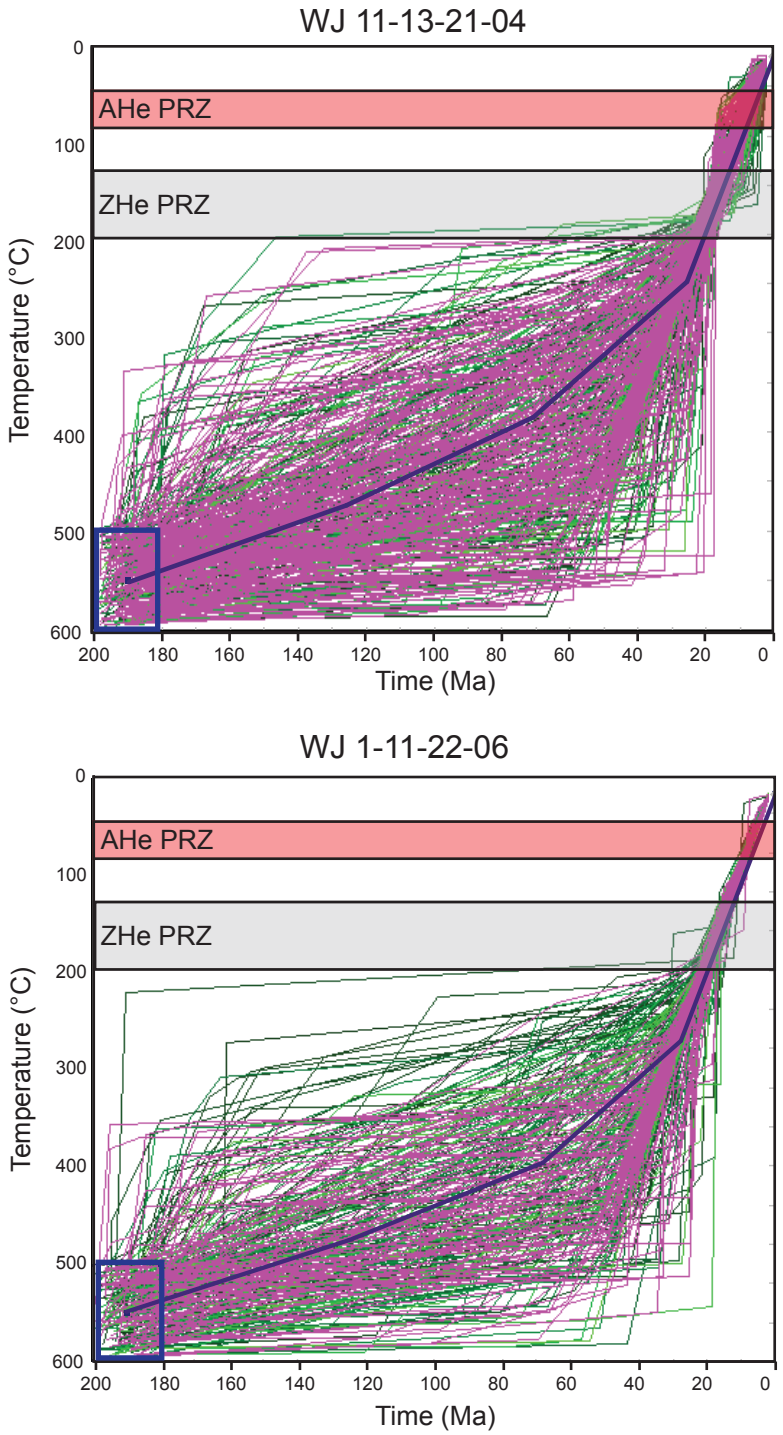


Figure 17. Inverse modeling of two samples using HeFTy showing good (green) and acceptable (purple) possible exhumation paths, see text for discussion. Blue box in lower left of plots are initial boundary conditions of >500°C before 180 Ma. The blue line shows the weighted mean path of exhumation. Grey and red boxes show the temperature ranges for zircon He partial retention zone, and the apatite He partial retention zones respectively. (A) Sample WJ 11-13-21-04. (B) Sample WJ 1-11-22-06.

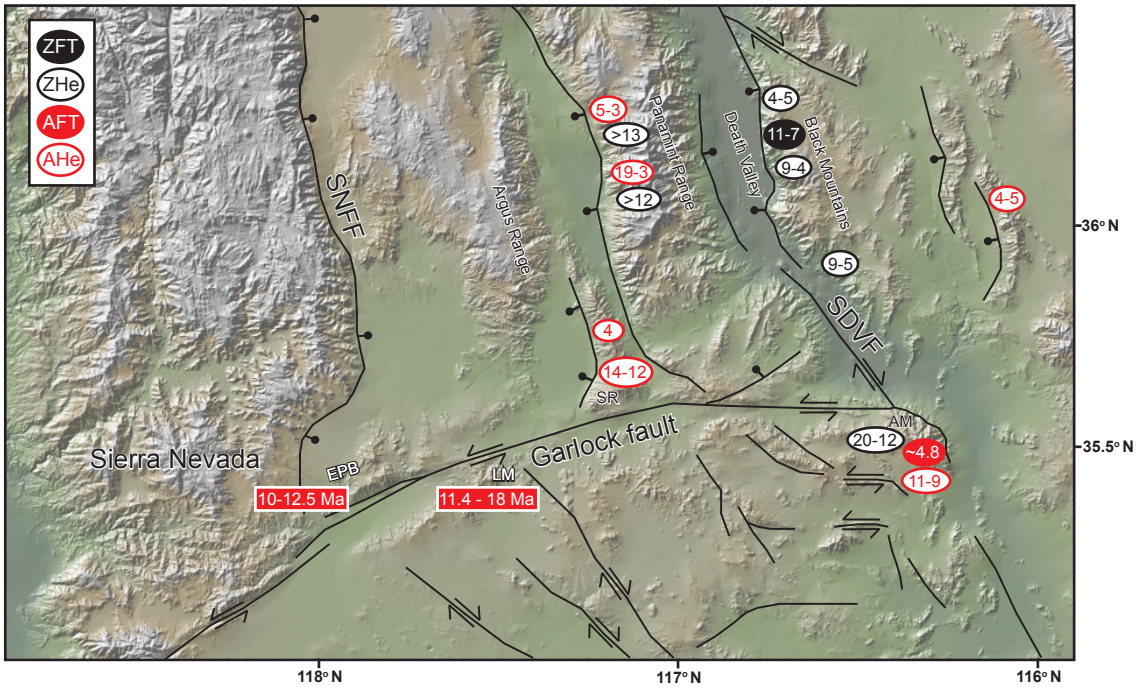


Figure 18. Compilation of cooling events recorded in low-temperature thermochronology data from the Death Valley and surrounding areas. Ages in circles are the interpreted cooling ages from previous studies. Black filled circles are cooling ages recorded by zircon fission track ages. Black open circles are zircon He cooling ages. Red filled circles are apatite fission track cooling ages. Red open circles are apatite He cooling ages. Red boxes are estimates for the initation of left-slip faulting at locations along the Garlock fault. Data Sources: Avawatz Mountains - Reinert (2004), Chinn (2013), This study; Southern Black Mountains - Bidgoli et al. (2015); Northern Black Mountains - Holm and Dokka (1993), Bidgoli et al. (2015); Funeral Mountains - Holm and Dokka (1991); Panamint Range - Bidgoli et al. (2015); Slate Range- Walker et al. (2014); El Paso Basin- Burbank and Whistler (1987), Sample (2018); Lava Mountains- (Andrew et al., 2014).

| Sample | Latitude | Longitude | Elevation (m) | AHe | ZHe |
|---|---|---|---|---|---|
| WJ 11-14-21-01 | 35.514807 | -116.252416 | 630 | 6.9 ± 2.6 | 12.3 ± 6.3 |
| WJ 11-13-21-03 | 35.517905 | -116.256115 | 650 | 6.8 ± 1.7 | 16.5 ± 3.2 |
| WJ 1-11-22-06 | 35.526848 | -116.263312 | 810 | 7.2 ± 2.0 | 14.0 ± 2.8 |
| WJ 11-13-21-04 | 35.514575 | -116.285568 | 1010 | *5.7 ± 4.2 | 17.2 ± 4.3 |
| WJ 1-11-22-04 | 35.525651 | -116.278521 | 1180 | 4.8 ± 1.3 | 14.7 ± 2.8 |
| WJ 1-11-22-03 | 35.525668 | -116.286076 | 1365 | 5.1 ± 0.1 | 14.1 ± 3.3 |
| WJ 1-11-22-02 | 35.524886 | -116.29248 | 1524 | *6.3 ± 1.5 | 13.8 ± 5.1 |
| WJ 11-13-21-06 | 35.5147 | -116.303763 | 1580 | *6.1 ± 3.2 | 49.3 ± 6.3 |
| WJ 1-11-22-01 | 35.526413 | -116.300816 | 1761 | *6.4 ± 1.0 | 15.3 ± 2.5 |
| WJ 1-10-22-01 | 35.512418 | -116.330833 | 1850 | 6.8 ± 0.7 | 79.4 ± 22 |

Table 1: Summary table of (U-Th)/He data from eastern transect across the Mule Spring fault. Errors for apatite helium (AHe) and zircon helium (ZHe) ages are 2 sigma errors. AHe ages marked with an asterisk are ages supplemented by additional samples from this study, all other AHe ages are from Reinert (2004).

| Sample Name and Aliquot | length 1 (μm) [c] | width 1 (μm) [c] | length 2 (μm) [c] | width 2 (μm) [c] | Geometry [e] | Np [f] | 4He (fmol) [g] | ± [h] | U (ng) [i] | ± [h] | Th (ng) [j] | ± [h] | 147Sm (ng) [k] | ± [h] |
|---|---|---|---|---|---|---|---|---|---|---|---|---|---|---|
| **1-11-22-04** | | | | | | | | | | | | | | |
| Z01 | 268.4 | 105.0 | 265.8 | 84.2 | Orthorhombic | Doubly terminated | 133.480 | 1.241 | 1.980 | 0.057 | 1.420 | 0.034 | n.m. | n.m |
| Z02 | 286.6 | 89.4 | 287.6 | 59.4 | Orthorhombic | Doubly terminated | 102.250 | 0.894 | 1.260 | 0.022 | 1.250 | 0.025 | n.m. | n.m |
| Z03 | 287.6 | 120.1 | 288.8 | 69.0 | Orthorhombic | Doubly terminated | 191.280 | 1.165 | 2.420 | 0.054 | 2.150 | 0.094 | n.m. | n.m |
| **1-11-22-06** | | | | | | | | | | | | | | |
| Z01 | 395.1 | 144.6 | 394.9 | 97.9 | Orthorhombic | Doubly terminated | 571.000 | 4.846 | 7.420 | 0.186 | 4.210 | 0.331 | n.m. | n.m |
| Z02 | 324.8 | 156.3 | 322.5 | 119.0 | Orthorhombic | Doubly terminated | 643.870 | 6.294 | 8.310 | 0.170 | 4.060 | 0.295 | n.m. | n.m |
| Z03 | 314.4 | 213.5 | 277.7 | 142.7 | Orthorhombic | Doubly terminated | 723.100 | 5.890 | 11.200 | 0.099 | 4.670 | 0.130 | n.m. | n.m |
| **1-11-22-02** | | | | | | | | | | | | | | |
| Z01 | 267.4 | 124.2 | 267.4 | 94.0 | Orthorhombic | Doubly terminated | 220.120 | 2.162 | 2.650 | 0.078 | 1.750 | 0.042 | n.m. | n.m |
| Z02 | 293.6 | 138.0 | 298.5 | 73.8 | Orthorhombic | Doubly terminated | 225.690 | 1.553 | 4.210 | 0.082 | 1.840 | 0.050 | n.m. | n.m |
| Z03 | 334.7 | 131.3 | 332.1 | 136.1 | Orthorhombic | Doubly terminated | 320.070 | 2.433 | 4.180 | 0.086 | 2.580 | 0.067 | n.m. | n.m |
| **1-11-22-03** | | | | | | | | | | | | | | |
| Z01 | 268.8 | 114.2 | 263.2 | 87.0 | Orthorhombic | Doubly terminated | 562.640 | 6.467 | 7.690 | 0.138 | 1.460 | 0.075 | n.m. | n.m |
| Z02 | 209.7 | 128.2 | 209.9 | 94.5 | Orthorhombic | Doubly terminated | 143.330 | 1.118 | 2.290 | 0.073 | 1.240 | 0.031 | n.m. | n.m |
| Z03 | 233.6 | 141.7 | 233.9 | 83.5 | Orthorhombic | Doubly terminated | 241.140 | 1.998 | 3.480 | 0.066 | 1.600 | 0.053 | n.m. | n.m |
| **11-13-21-06** | | | | | | | | | | | | | | |
| Z01 | 178.6 | 80.3 | 194.0 | 52.2 | Orthorhombic | Doubly terminated | 130.840 | 0.711 | 0.605 | 0.024 | 0.532 | 0.017 | n.m. | n.m |
| Z02 | 296.7 | 113.7 | 295.0 | 100.0 | Orthorhombic | Doubly terminated | 1013.400 | 10.557 | 3.560 | 0.036 | 3.480 | 0.027 | n.m. | n.m |
| Z03 | 239.4 | 86.6 | 235.9 | 72.5 | Orthorhombic | Doubly terminated | 269.760 | 2.121 | 1.050 | 0.023 | 0.862 | 0.041 | n.m. | n.m |
| **1-11-22-01** | | | | | | | | | | | | | | |
| Z01 | 285.6 | 177.8 | 285.2 | 110.5 | Orthorhombic | Doubly terminated | 364.300 | 2.609 | 4.300 | 0.089 | 3.930 | 0.201 | n.m. | n.m |
| Z02 | 333.3 | 120.4 | 346.2 | 118.3 | Orthorhombic | Doubly terminated | 475.390 | 4.261 | 6.330 | 0.150 | 4.300 | 0.085 | n.m. | n.m |
| Z03 | 383.3 | 144.9 | 335.3 | 133.2 | Orthorhombic | Doubly terminated | 551.780 | 4.448 | 6.180 | 0.177 | 3.750 | 0.023 | n.m. | n.m |
| **11-14-21-01** | | | | | | | | | | | | | | |
| Z01 | 286.6 | 97.7 | 299.8 | 71.0 | Orthorhombic | Doubly terminated | 119.180 | 0.845 | 2.090 | 0.033 | 1.430 | 0.044 | n.m. | n.m |
| Z02 | 308.0 | 122.2 | 305.1 | 102.9 | Orthorhombic | Doubly terminated | 227.160 | 1.795 | 4.550 | 0.056 | 2.540 | 0.080 | n.m. | n.m |
| Z03 | 321.1 | 99.2 | 324.4 | 126.3 | Orthorhombic | Doubly terminated | 303.800 | 1.614 | 3.600 | 0.138 | 2.610 | 0.055 | n.m. | n.m |
| **1-10-22-01** | | | | | | | | | | | | | | |
| Z01 | 96.3 | 57.8 | 96.9 | 59.7 | Orthorhombic | Single termination | 118.610 | 0.510 | 0.358 | 0.020 | 0.114 | 0.008 | n.m. | n.m |
| Z02 | 122.4 | 53.8 | 129.8 | 55.3 | Orthorhombic | Single termination | 138.300 | 0.988 | 0.349 | 0.006 | 0.357 | 0.014 | n.m. | n.m |
| Z03 | 116.3 | 61.0 | 135.1 | 62.7 | Orthorhombic | Single termination | 134.440 | 0.798 | 0.425 | 0.014 | 0.429 | 0.020 | n.m. | n.m |
| **11-13-21-03** | | | | | | | | | | | | | | |
| Z01 | 277.0 | 116.5 | 277.0 | 118.5 | Orthorhombic | Doubly terminated | 181.660 | 1.087 | 2.120 | 0.052 | 2.240 | 0.061 | n.m. | n.m |
| Z02 | 323.5 | 105.8 | 324.2 | 100.1 | Orthorhombic | Doubly terminated | 252.817 | 2.613 | 2.820 | 0.096 | 2.840 | 0.023 | n.m. | n.m |
| Z03 | 340.9 | 176.3 | 339.3 | 131.2 | Orthorhombic | Doubly terminated | 938.231 | 7.211 | 9.410 | 0.107 | 6.220 | 0.194 | n.m. | n.m |
| **11-13-21-04** | | | | | | | | | | | | | | |
| Z01 | 280.2 | 101.8 | 276.9 | 95.6 | Orthorhombic | Doubly terminated | 879.537 | 8.215 | 11.000 | 0.157 | 2.490 | 0.438 | n.m. | n.m |
| Z02 | 318.6 | 93.9 | 330.5 | 125.9 | Orthorhombic | Doubly terminated | 638.109 | 5.111 | 8.420 | 0.167 | 1.720 | 0.045 | n.m. | n.m |
| Z03 | 177.5 | 73.2 | 177.5 | 90.2 | Orthorhombic | Doubly terminated | 211.351 | 1.595 | 2.370 | 0.069 | 0.567 | 0.042 | n.m. | n.m |
| Z04 | 261.6 | 109.6 | 255.8 | 132.9 | Orthorhombic | Doubly terminated | 426.748 | 5.680 | 0.198 | 1.580 | 0.050 | 0.050 | n.m. | n.m |
| Z05 | 330.0 | 173.5 | 327.7 | 166.0 | Orthorhombic | Doubly terminated | 820.808 | 21.400 | 0.142 | 4.590 | 0.141 | 0.141 | n.m. | n.m |

Table A1.1: Zircon (U-Th)/He analyses from across the eastern rangefront of the Avawatz Mountains. This table follows the recommendations and approach of Flowers et al. (2022).

| Sample Name and Aliquot | Rs (μm) [l] | Mass (μg) [m] | 4He (nmol/g) [n] | ± [o] | U (ppm) [n] | ± [o] | Th (ppm) [n] | ± [o] | Sm (ppm) [n] | ± [o] | eU [p] | ± [q] | Uncorr Date (Ma) [r] | Uncorr Date Analytical ± (Ma) 2s [s] | Combined Ft [t] | Corrected Date (Ma) [u] | ± TAU (Ma) 2σ [v] | ± TAU+Ft (Ma) 2σ [v] |
|---|---|---|---|---|---|---|---|---|---|---|---|---|---|---|---|---|---|---|
| **1-11-22-04** | | | | | | | | | | | | | | | | | | |
| Z01 | 59.7 | 8.4 | 712.383 | 6.623 | 236.9 | 6.8 | 169.9 | 4.1 | n.m. | n.m | 279.0 | 41.9 | 10.6 | 0.1 | 0.81 | 13.2 | 0.2 | 0.2 |
| Z02 | 48.0 | 5.8 | 783.412 | 6.852 | 216.4 | 3.7 | 214.7 | 4.3 | n.m. | n.m | 269.0 | 40.4 | 12.1 | 0.1 | 0.76 | 15.9 | 0.1 | 0.1 |
| Z03 | 57.0 | 8.5 | 999.666 | 6.086 | 283.5 | 6.3 | 251.8 | 11.0 | n.m. | n.m | 345.5 | 51.8 | 12.0 | 0.1 | 0.80 | 15.1 | 0.2 | 0.2 |
| **1-11-22-06** | | | | | | | | | | | | | | | | | | |
| Z01 | 76.6 | 20.5 | 1241.793 | 10.538 | 361.7 | 9.1 | 205.2 | 16.1 | n.m. | n.m | 413.1 | 62.0 | 12.5 | 0.2 | 0.85 | 14.7 | 0.2 | 0.2 |
| Z02 | 82.9 | 19.9 | 1441.603 | 14.093 | 417.0 | 8.5 | 203.7 | 14.8 | n.m. | n.m | 468.5 | 70.3 | 12.8 | 0.1 | 0.86 | 14.9 | 0.2 | 0.2 |
| Z03 | 93.1 | 24.6 | 1313.269 | 10.697 | 455.9 | 4.0 | 190.1 | 5.3 | n.m. | n.m | 504.5 | 75.7 | 10.8 | 0.1 | 0.88 | 12.4 | 0.1 | 0.1 |
| **1-11-22-02** | | | | | | | | | | | | | | | | | | |
| Z01 | 66.4 | 10.5 | 935.175 | 9.184 | 252.3 | 7.4 | 166.6 | 4.0 | n.m. | n.m | 293.8 | 44.1 | 13.2 | 0.2 | 0.83 | 16.0 | 0.2 | 0.2 |
| Z02 | 61.6 | 10.4 | 964.403 | 6.635 | 403.2 | 7.8 | 176.2 | 4.8 | n.m. | n.m | 448.1 | 67.2 | 8.9 | 0.1 | 0.81 | 11.0 | 0.1 | 0.1 |
| Z03 | 83.2 | 20.3 | 703.629 | 5.348 | 206.0 | 4.2 | 127.1 | 3.3 | n.m. | n.m | 237.7 | 35.7 | 12.3 | 0.1 | 0.86 | 14.3 | 0.1 | 0.1 |
| **1-11-22-03** | | | | | | | | | | | | | | | | | | |
| Z01 | 62.3 | 9.1 | 2746.229 | 31.564 | 841.3 | 15.1 | 159.7 | 8.2 | n.m. | n.m | 885.4 | 132.8 | 12.9 | 0.1 | 0.82 | 15.8 | 0.2 | 0.2 |
| Z02 | 62.4 | 7.6 | 846.556 | 6.605 | 303.2 | 9.6 | 164.2 | 4.1 | n.m. | n.m | 344.4 | 51.7 | 10.2 | 0.2 | 0.82 | 12.5 | 0.2 | 0.2 |
| Z03 | 62.4 | 8.5 | 1264.038 | 10.475 | 408.9 | 7.8 | 188.0 | 6.2 | n.m. | n.m | 456.6 | 68.5 | 11.5 | 0.1 | 0.82 | 14.1 | 0.1 | 0.1 |
| **11-13-21-06** | | | | | | | | | | | | | | | | | | |
| Z01 | 40.5 | 2.7 | 2131.723 | 11.579 | 220.9 | 8.6 | 194.3 | 6.4 | n.m. | n.m | 268.8 | 40.3 | 32.9 | 0.5 | 0.72 | 45.7 | 0.8 | 0.8 |
| Z02 | 67.8 | 11.9 | 3811.941 | 39.711 | 300.1 | 3.0 | 293.4 | 2.3 | n.m. | n.m | 372.1 | 55.8 | 42.5 | 0.3 | 0.83 | 51.3 | 0.3 | 0.3 |
| Z03 | 51.0 | 5.4 | 2237.624 | 17.594 | 195.2 | 4.3 | 160.3 | 7.6 | n.m. | n.m | 234.8 | 35.2 | 39.5 | 0.4 | 0.78 | 51.0 | 0.6 | 0.5 |
| **1-11-22-01** | | | | | | | | | | | | | | | | | | |
| Z01 | 79.6 | 16.9 | 961.394 | 6.884 | 254.3 | 5.3 | 232.5 | 11.9 | n.m. | n.m | 311.5 | 46.7 | 12.8 | 0.1 | 0.85 | 15.1 | 0.2 | 0.2 |
| Z02 | 76.4 | 17.2 | 1230.850 | 11.032 | 367.3 | 8.7 | 249.5 | 5.0 | n.m. | n.m | 429.4 | 64.4 | 11.9 | 0.1 | 0.85 | 14.1 | 0.2 | 0.2 |
| Z03 | 87.1 | 23.9 | 1029.497 | 8.300 | 258.4 | 7.4 | 156.8 | 1.0 | n.m. | n.m | 297.6 | 44.6 | 14.4 | 0.2 | 0.87 | 16.6 | 0.2 | 0.2 |
| **11-14-21-01** | | | | | | | | | | | | | | | | | | |
| Z01 | 54.5 | 7.6 | 699.251 | 4.958 | 274.8 | 4.3 | 188.1 | 5.8 | n.m. | n.m | 321.6 | 48.2 | 9.1 | 0.1 | 0.79 | 11.5 | 0.1 | 0.1 |
| Z02 | 70.9 | 13.5 | 750.330 | 5.930 | 336.9 | 4.2 | 188.0 | 5.9 | n.m. | n.m | 384.1 | 57.6 | 8.1 | 0.1 | 0.84 | 9.7 | 0.1 | 0.1 |
| Z03 | 71.2 | 14.4 | 943.387 | 5.011 | 250.6 | 9.6 | 181.7 | 3.8 | n.m. | n.m | 295.6 | 44.3 | 13.3 | 0.2 | 0.84 | 15.8 | 0.3 | 0.3 |
| **1-10-22-01** | | | | | | | | | | | | | | | | | | |
| Z01 | 33.0 | 1.2 | 4282.509 | 18.413 | 289.7 | 16.1 | 92.3 | 6.7 | n.m. | n.m | 313.8 | 47.1 | 56.5 | 1.5 | 0.67 | 83.8 | 2.2 | 2.2 |
| Z02 | 33.5 | 1.5 | 4133.094 | 29.517 | 233.8 | 4.0 | 239.1 | 9.2 | n.m. | n.m | 292.4 | 43.9 | 58.6 | 0.5 | 0.67 | 87.2 | 0.7 | 0.8 |
| Z03 | 36.9 | 1.9 | 3209.583 | 19.056 | 227.4 | 7.4 | 229.6 | 10.6 | n.m. | n.m | 283.7 | 42.6 | 46.9 | 0.7 | 0.70 | 67.1 | 1.0 | 0.9 |
| **11-13-21-03** | | | | | | | | | | | | | | | | | | |
| Z01 | 72.2 | 12.8 | 635.532 | 3.804 | 166.2 | 4.1 | 175.6 | 4.8 | n.m. | n.m | 209.2 | 31.4 | 12.6 | 0.1 | 0.84 | 15.1 | 0.2 | 0.2 |
| Z02 | 67.0 | 12.6 | 897.636 | 9.277 | 224.4 | 7.6 | 226.0 | 1.8 | n.m. | n.m | 279.8 | 42.0 | 13.3 | 0.2 | 0.83 | 16.1 | 0.2 | 0.2 |
| Z03 | 90.8 | 25.3 | 1651.360 | 12.692 | 371.2 | 4.2 | 245.4 | 7.7 | n.m. | n.m | 432.3 | 64.8 | 15.9 | 0.1 | 0.87 | 18.2 | 0.1 | 0.1 |
| **11-13-21-04** | | | | | | | | | | | | | | | | | | |
| Z01 | 63.0 | 9.6 | 4077.018 | 38.082 | 1142.9 | 16.3 | 258.7 | 45.5 | n.m. | n.m | 1212.7 | 181.9 | 14.0 | 0.1 | 0.82 | 17.1 | 0.2 | 0.2 |
| Z02 | 69.4 | 13.7 | 2072.164 | 16.598 | 612.8 | 12.2 | 125.2 | 3.3 | n.m. | n.m | 647.1 | 97.1 | 13.3 | 0.1 | 0.84 | 15.9 | 0.2 | 0.2 |
| Z03 | 48.5 | 3.8 | 2507.194 | 18.922 | 630.2 | 18.3 | 150.8 | 11.2 | n.m. | n.m | 670.6 | 100.6 | 15.5 | 0.2 | 0.77 | 20.2 | 0.3 | 0.3 |
| Z04 | 71.8 | 12.0 | 1586.508 | 13.880 | 473.3 | 16.5 | 131.7 | 4.2 | n.m. | n.m | 508.1 | 76.2 | 13.0 | 0.2 | 0.84 | 15.4 | 0.3 | 0.3 |
| Z05 | 98.3 | 28.9 | 1268.123 | 10.414 | 741.0 | 4.9 | 158.9 | 4.9 | n.m. | n.m | 784.3 | 117.6 | 6.7 | 0.0 | 0.88 | 7.6 | 0.0 | 0.0 |

Table A1.2: Zircon (U-Th)/He analyses from across the eastern rangefront of the Avawatz Mountains. This table follows the recommendations and approach of Flowers et al. (2022).

| Sample Name and Aliquot | length 1 (µm) [c] | width 1 (µm) [c] | length 2 (µm) [c] | width 2 (µm) [c] | Geometry [e] | Np [f] | 4He (fmol) [g] | ± [h] | U (ng) [i] | ± [h] | Th (ng) [j] | ± [h] | 147Sm (ng) [k] | ± [h] |
|---|---|---|---|---|---|---|---|---|---|---|---|---|---|---|
| **11-13-21-04** | | | | | | | | | | | | | | |
| A01 | 135.1 | 77.4 | 130.9 | 47.8 | Hexagonal | Single termination | 0.063 | 0.017 | 0.000 | 0.000 | 0.000 | 0.000 | 0.000 | 0.000 |
| A02 | 150.2 | 66.2 | 146.6 | 40.9 | Hexagonal | Single termination | 0.050 | 0.009 | 0.003 | 0.000 | 0.004 | 0.001 | 0.008 | 0.001 |
| A03 | 158.6 | 75.9 | 157.8 | 54.1 | Hexagonal | Single termination | 0.116 | 0.011 | 0.008 | 0.000 | 0.008 | 0.001 | 0.012 | 0.001 |
| A04 | 126.2 | 101.8 | 127.4 | 54.9 | Hexagonal | Single termination | 0.224 | 0.009 | 0.008 | 0.000 | 0.010 | 0.001 | 0.015 | 0.001 |
| **11-13-21-06** | | | | | | | | | | | | | | |
| A01 | 142.4 | 145.9 | 142.4 | 144.2 | Hexagonal | Single termination | 4.677 | 0.044 | 0.144 | 0.003 | 0.080 | 0.002 | 0.063 | 0.002 |
| A02 | 166.1 | 135.7 | 176.7 | 107.0 | Hexagonal | Single termination | 4.202 | 0.033 | 0.110 | 0.004 | 0.128 | 0.004 | 0.052 | 0.001 |
| A03 | 199.4 | 130.2 | 202.5 | 88.4 | Hexagonal | Single termination | 0.0000 | 0.0000 | 0.2370 | 0.0072 | 0.1590 | 0.0038 | 0.1010 | 0.0018 |
| A04 | 164.5 | 114.2 | 152.4 | 90.9 | Hexagonal | Single termination | 3.2430 | 0.0288 | 0.1150 | 0.0058 | 0.0590 | 0.0041 | 0.0410 | 0.0022 |
| A05 | 176.9 | 121.3 | 174.7 | 100.3 | Hexagonal | Doubly terminated | 5.5260 | 0.0324 | 0.1560 | 0.0044 | 0.0980 | 0.0059 | 0.0630 | 0.0005 |
| **WJ 1-11-22(01)** | | | | | | | | | | | | | | |
| A02 | 126.2 | 115.4 | 128.6 | 109.3 | Hexagonal | Single termination | 12.901 | 0.075 | 0.4010 | 0.0093 | 0.2940 | 0.0074 | 0.0600 | 0.0036 |
| A03 | 96.9 | 111.7 | 131.9 | 98.6 | Hexagonal | No terminations | 20.141 | 0.139 | 0.5960 | 0.0053 | 0.6560 | 0.0168 | 0.0560 | 0.0018 |
| A04 | 120.6 | 94.1 | 120.3 | 80.7 | Hexagonal | Single termination | 10.132 | 0.064 | 0.0000 | 0.0002 | 0.0000 | 0.0000 | 0.0000 | 0.0000 |
| A05 | 136.3 | 113.4 | 160.9 | 100.3 | Hexagonal | No terminations | 14.752 | 0.117 | 0.4570 | 0.0096 | 0.5300 | 0.0115 | 0.0760 | 0.0026 |
| A01 | 143.5 | 96.4 | 143.5 | 96.4 | Hexagonal | Single termination | 7.379 | 0.056 | 0.2500 | 0.0087 | 0.2720 | 0.0063 | 0.0490 | 0.0017 |
| **WJ 1-11-22(02)** | | | | | | | | | | | | | | |
| A01 | 184.9 | 124.3 | 184.3 | 111.1 | Hexagonal | Single termination | 40.870 | 0.258 | 1.1900 | 0.0279 | 1.1300 | 0.0376 | 0.1330 | 0.0054 |
| A02 | 148.3 | 107.6 | 142.6 | 80.9 | Hexagonal | Single termination | 11.711 | 0.081 | 0.4180 | 0.0192 | 0.3800 | 0.0057 | 0.0510 | 0.0022 |
| A03 | 166.5 | 81.0 | 169.3 | 105.4 | Hexagonal | Single termination | 8.018 | 0.070 | 0.2580 | 0.0100 | 0.2860 | 0.0084 | 0.0480 | 0.0007 |
| A04 | 137.7 | 67.4 | 136.8 | 52.4 | Hexagonal | Doubly terminated | 2.308 | 0.024 | 0.1000 | 0.0040 | 0.1300 | 0.0020 | 0.0420 | 0.0034 |
| A05 | 146.6 | 118.4 | 144.4 | 99.4 | Hexagonal | No terminations | 10.574 | 0.081 | 0.3340 | 0.0114 | 0.4060 | 0.0138 | 0.0540 | 0.0019 |

| Sample Name and Aliquot | Rs (µm) [l] | Mass (µg) [m] | 4He (nmol/g) [n] | ± [o] | U (ppm) [n] | ± [o] | Th (ppm) [n] | ± [o] | Sm (ppm) [n] | ± [o] | eU [p] | Uncorr Date (Ma) [r] | Uncorr Date Analytical ± (Ma) 2s [s] | Combined Ft [t] | Corrected Date (Ma) [u] | ± TAU (Ma) 2σ [v] |
|---|---|---|---|---|---|---|---|---|---|---|---|---|---|---|---|---|
| **11-13-21-04** | | | | | | | | | | | | | | | | |
| A01 | 27.8 | 0.7 | 3.854 | 1.010 | 0.1 | 0.2 | 0.0 | 0.0 | 0.0 | 0.0 | 0.1 | 141.2 | N/A | N/A | N/A | N/A |
| A02 | 24.6 | 0.6 | 3.590 | 0.615 | 4.1 | 0.6 | 6.1 | 1.4 | 12.4 | 1.8 | 5.6 | 2.6 | 0.3 | 0.5 | 5.5 | 0.6 |
| A03 | 32.4 | 1.1 | 4.745 | 0.454 | 7.1 | 0.2 | 7.6 | 1.2 | 11.0 | 1.0 | 8.9 | 2.2 | 0.1 | 0.6 | 3.7 | 0.2 |
| A04 | 29.6 | 0.9 | 11.234 | 0.447 | 8.7 | 0.3 | 11.1 | 1.3 | 17.4 | 1.4 | 11.4 | 4.1 | 0.1 | 0.5 | 7.9 | 0.2 |
| **11-13-21-06** | | | | | | | | | | | | | | | | |
| A01 | 61.9 | 4.7 | 44.514 | 0.422 | 30.7 | 0.5 | 17.1 | 0.4 | 13.4 | 0.3 | 35.0 | 5.3 | 0.0 | 0.8 | 6.8 | 0.1 |
| A02 | 56.5 | 4.0 | 46.911 | 0.370 | 27.5 | 0.9 | 32.0 | 1.0 | 13.0 | 0.1 | 35.4 | 5.5 | 0.1 | 0.8 | 7.3 | 0.1 |
| A03 | 53.1 | 3.597 | 0.00 | 0.00 | 65.9 | 2.0 | 44.2 | 1.1 | 28.1 | 0.5 | 76.9 | 0.0 | 0.0 | 0.73 | 0.0 | 0.0 |
| A04 | 50.9 | 2.715 | 53.30 | 0.47 | 42.4 | 2.1 | 21.7 | 1.5 | 15.2 | 0.8 | 47.9 | 4.6 | 0.1 | 0.72 | 6.4 | 0.2 |
| A05 | 55.1 | 2.789 | 88.40 | 0.52 | 55.9 | 1.6 | 35.2 | 2.1 | 22.7 | 0.2 | 64.7 | 5.7 | 0.1 | 0.74 | 7.7 | 0.1 |
| **WJ 1-11-22(01)** | | | | | | | | | | | | | | | | |
| A02 | 53.2 | 2.6 | 219.46 | 1.27 | 152.9 | 3.6 | 112.1 | 2.8 | 23.0 | 1.4 | 180.7 | 5.0 | 0.1 | 0.73 | 6.9 | 0.1 |
| A03 | 51.7 | 2.7 | 331.07 | 2.28 | 219.6 | 1.9 | 241.7 | 6.2 | 20.4 | 0.7 | 278.7 | 4.9 | 0.0 | 0.72 | 6.9 | 0.1 |
| A04 | 41.6 | 1.5 | 297.15 | 1.88 | 0.0 | 0.1 | 0.0 | 0.0 | 0.0 | 0.0 | 0.0 | N/A | N/A | 0.68 | N/A | N/A |
| A05 | 55.9 | 3.6 | 180.62 | 1.43 | 125.4 | 2.6 | 145.4 | 3.2 | 20.8 | 0.7 | 161.0 | 4.7 | 0.1 | 0.74 | 6.3 | 0.1 |
| A01 | 51.7 | 2.4 | 136.29 | 1.03 | 103.5 | 3.6 | 112.6 | 2.6 | 20.2 | 0.7 | 131.1 | 4.3 | 0.1 | 0.72 | 6.0 | 0.2 |
| **WJ 1-11-22(02)** | | | | | | | | | | | | | | | | |
| A01 | 60.4 | 4.5 | 407.98 | 2.58 | 266.3 | 6.2 | 252.8 | 8.4 | 29.8 | 1.2 | 328.4 | 5.2 | 0.1 | 0.76 | 6.8 | 0.1 |
| A02 | 46.3 | 2.0 | 258.00 | 1.79 | 206.4 | 9.5 | 187.6 | 2.8 | 25.1 | 1.1 | 252.6 | 4.2 | 0.2 | 0.69 | 6.2 | 0.2 |
| A03 | 53.7 | 2.9 | 121.43 | 1.06 | 87.6 | 3.4 | 97.1 | 2.8 | 16.3 | 0.2 | 111.3 | 4.5 | 0.1 | 0.73 | 6.2 | 0.2 |
| A04 | 32.2 | 0.7 | 141.77 | 1.49 | 137.7 | 5.5 | 179.0 | 2.7 | 58.2 | 4.7 | 181.4 | 3.2 | 0.1 | 0.56 | 5.8 | 0.2 |
| A05 | 56.0 | 3.6 | 131.31 | 1.00 | 93.0 | 3.2 | 113.0 | 3.8 | 15.2 | 0.5 | 120.5 | 4.5 | 0.1 | 0.74 | 6.2 | 0.2 |

Table A2: Apatite (U-Th)/He analyses from across the eastern rangefront of the Avawatz Mountains. This table follows the recommendations and approach of Flowers et al. (2022).

| **Sample** | **11-12-21-01** | **11-12-21-02** | **11-13-21-01** | **11-13-21-02** | **11-14-21-01** | **3-16-22-01** |
|---|---|---|---|---|---|---|
| Rock type | Felsic Sill; pCp | Mafic Intrusion; pCp | Avawatz granodiorite | Granite | Avawatz granodiorite | Tertiary extrusive |
| Latitude | 35.595758 | 35.594523 | 35.580512 | 35.571692 | 35.514773 | 35.60967 |
| Longitude | -116.361926 | -116.360369 | -116.328743 | -116.329568 | -116.252236 | -116.402215 |
| | | | | | | |
| SiO2 (%) | 72.6 | 47.9 | 61.2 | 73 | 57.9 | 69.2 |
| Al2O3 (%) | 14.3 | 17.85 | 16.45 | 14.45 | 16.25 | 12.5 |
| Fe2O3 (%) | 2.55 | 9.35 | 6.76 | 2.21 | 8.14 | 6.18 |
| CaO (%) | 1.32 | 8.52 | 5.28 | 2.12 | 5.4 | 1.09 |
| MgO (%) | 0.68 | 7.46 | 2.49 | 0.45 | 3.51 | 2.47 |
| Na2O (%) | 2.9 | 2.81 | 2.89 | 3.3 | 2.86 | 1.84 |
| K2O (%) | 4.61 | 1.42 | 2.55 | 3.68 | 4.24 | 4.38 |
| Cr2O3 (%) | 0.004 | 0.03 | 0.003 | <0.002 | 0.005 | 0.018 |
| TiO2 (%) | 0.33 | 1.66 | 0.68 | 0.2 | 0.93 | 0.78 |
| MnO (%) | 0.02 | 0.12 | 0.12 | 0.09 | 0.15 | 0.06 |
| P2O5 (%) | 0.06 | 0.24 | 0.16 | 0.08 | 0.35 | 0.17 |
| SrO (%) | 0.02 | 0.05 | 0.03 | 0.02 | 0.06 | 0.01 |
| BaO (%) | 0.11 | 0.03 | 0.07 | 0.08 | 0.1 | 0.08 |
| LOI (%) | 1.45 | 2.27 | 1.12 | 1.32 | 1.54 | 1.13 |
| Total (%) | 100.95 | 99.71 | 99.8 | 101 | 101.44 | 99.91 |
| | | | | | | |
| Ba (ppm) | 983 | 266 | 646 | 705 | 877 | 659 |
| Ce (ppm) | 84.6 | 22.4 | 63.9 | 51.5 | 102 | 104 |
| Cr (ppm) | 30 | 210 | 20 | 10 | 30 | 127 |
| Cs (ppm) | 2.54 | 2.4 | 1.31 | 1.61 | 1.12 | 3.04 |
| Dy (ppm) | 6.03 | 3.48 | 4.05 | 3.41 | 5.54 | 7.4 |
| Er (ppm) | 3.57 | 2.13 | 2.7 | 2.08 | 3.38 | 4.8 |
| Eu (ppm) | 1.15 | 1.25 | 1.26 | 0.76 | 1.77 | 1.26 |
| Ga (ppm) | 16.2 | 17.2 | 18.8 | 16 | 19.9 | 16 |
| Gd (ppm) | 5.62 | 4.05 | 4.24 | 3.3 | 7.07 | 7.39 |
| Hf (ppm) | 7.7 | 2.5 | 5.7 | 4 | 6.7 | 9.64 |
| Ho (ppm) | 1.23 | 0.75 | 0.94 | 0.74 | 1.27 | 1.36 |
| La (ppm) | 41.1 | 9.2 | 32.2 | 26.5 | 45.6 | 46.2 |
| Lu (ppm) | 0.54 | 0.28 | 0.44 | 0.32 | 0.5 | 0.7 |
| Nb (ppm) | 13.2 | 5 | 7.3 | 10.4 | 13.2 | 14.35 |
| Nd (ppm) | 32.3 | 13.4 | 24.4 | 18.7 | 42.4 | 44.3 |
| Pr (ppm) | 9.13 | 3.06 | 7.04 | 5.53 | 11.8 | 11.8 |
| Rb (ppm) | 120 | 43 | 79.4 | 102.5 | 169 | 166.5 |
| Sm (ppm) | 6.1 | 3.44 | 4.73 | 3.9 | 8.57 | 9.54 |
| Sn (ppm) | 2 | 1 | 1 | 1 | 2 | 3.5 |
| Sr (ppm) | 204 | 438 | 317 | 197 | 559 | 82.4 |
| Ta (ppm) | 0.9 | 0.4 | 0.5 | 0.8 | 1.1 | 1 |
| Tb (ppm) | 0.95 | 0.59 | 0.72 | 0.56 | 1 | 1.2 |
| Th (ppm) | 15.15 | 1.29 | 7.88 | 12.4 | 34.4 | 25.6 |
| Tm (ppm) | 0.53 | 0.32 | 0.39 | 0.3 | 0.49 | 0.64 |
| U (ppm) | 1.8 | 0.71 | 0.96 | 1.42 | 6.04 | 3.22 |
| V (ppm) | 117 | 175 | 115 | 15 | 163 | 73 |
| W (ppm) | 2 | <1 | 1 | <1 | 1 | 1.2 |
| Y (ppm) | 33.6 | 18.8 | 23.2 | 20.2 | 32.2 | 37.3 |
| Yb (ppm) | 3.47 | 1.81 | 2.54 | 2.06 | 3.1 | 4.41 |
| Zr (ppm) | 283 | 97 | 214 | 136 | 243 | 341 |

Table A3.1: Geochemical analyses of samples from the Avawatz Mountains.

| **Sample** | **3-16-22-02** | **11-19-22-03** | **11-19-22-05** | **11-20-22-01** | **11-22-22-05** | **11-22-22-06** |
|---|---|---|---|---|---|---|
| Rock type | Quartz monzonite | Gneiss | Intrusion in Kingston Peak | Gneiss | Mesozoic intrusion | Mesozoic intrusion |
| Latitude | 35.581988 | 35.589561 | 35.597918 | 35.589417 | 35.606074 | 35.620097 |
| Longitude | -116.400559 | -116.372248 | -116.356556 | -116.360385 | -116.283724 | -116.28795 |
| | | | | | | |
| SiO2 (%) | 60.1 | 72.8 | 66 | 68.3 | 63 | 67.7 |
| Al2O3 (%) | 15.65 | 12.1 | 18.1 | 13.75 | 15.7 | 15.1 |
| Fe2O3 (%) | 7.07 | 3.21 | 3.88 | 2.87 | 6.23 | 3.04 |
| CaO (%) | 4.72 | 2 | 4.6 | 1.9 | 4.94 | 2.77 |
| MgO (%) | 2.43 | 0.68 | 1.2 | 0.66 | 2.45 | 0.55 |
| Na2O (%) | 3 | 2.7 | 2.93 | 0.62 | 2.61 | 3.06 |
| K2O (%) | 4.53 | 4.65 | 3.12 | 7.1 | 2.96 | 4.58 |
| Cr2O3 (%) | 0.007 | 0.008 | 0.009 | 0.008 | 0.012 | 0.011 |
| TiO2 (%) | 0.85 | 0.29 | 0.46 | 0.62 | 0.66 | 0.3 |
| MnO (%) | 0.13 | 0.05 | 0.05 | 0.07 | 0.09 | 0.05 |
| P2O5 (%) | 0.27 | 0.08 | 0.13 | 0.18 | 0.16 | 0.08 |
| SrO (%) | 0.06 | 0.01 | 0.04 | 0.01 | 0.03 | 0.02 |
| BaO (%) | 0.11 | 0.07 | 0.06 | 0.13 | 0.08 | 0.14 |
| LOI (%) | 1.4 | 2.36 | 1.29 | 3.18 | 0.94 | 0.62 |
| Total (%) | 100.33 | 101.01 | 101.87 | 99.4 | 99.86 | 98.02 |
| | | | | | | |
| Ba (ppm) | 863 | 685 | 579 | 1275 | 704 | 1355 |
| Ce (ppm) | 100 | 148.5 | 33.2 | 411 | 68.6 | 76.1 |
| Cr (ppm) | 51 | 57 | 58 | 60 | 86 | 78 |
| Cs (ppm) | 2.59 | 1.03 | 2.88 | 4.59 | 1.41 | 1.15 |
| Dy (ppm) | 6.12 | 5.58 | 4.27 | 9.9 | 4.75 | 4.66 |
| Er (ppm) | 3.42 | 2.21 | 2.73 | 4.46 | 2.94 | 2.73 |
| Eu (ppm) | 1.38 | 1.26 | 1.42 | 1.52 | 1.3 | 1.36 |
| Ga (ppm) | 20.3 | 15.8 | 16.2 | 18.1 | 17 | 14.8 |
| Gd (ppm) | 6.74 | 8.18 | 3.14 | 13.3 | 4.84 | 4.7 |
| Hf (ppm) | 7.92 | 8.55 | 8.32 | 15.95 | 6.68 | 6.41 |
| Ho (ppm) | 1.08 | 0.94 | 0.81 | 1.67 | 0.94 | 0.96 |
| La (ppm) | 49.4 | 73.1 | 16.2 | 198.5 | 33.8 | 39.2 |
| Lu (ppm) | 0.53 | 0.19 | 0.39 | 0.47 | 0.41 | 0.43 |
| Nb (ppm) | 18.85 | 10.1 | 9.44 | 27.5 | 9.29 | 9.71 |
| Nd (ppm) | 43.7 | 62.7 | 16.3 | 136 | 31.7 | 30.9 |
| Pr (ppm) | 11.65 | 16.65 | 3.9 | 39.2 | 7.57 | 8.21 |
| Rb (ppm) | 181 | 160 | 84.3 | 339 | 93.7 | 133.5 |
| Sm (ppm) | 8.59 | 11.5 | 3.92 | 21 | 6.28 | 5.66 |
| Sn (ppm) | 2.7 | 4.1 | 1.1 | 3.9 | 1.4 | 1.5 |
| Sr (ppm) | 529 | 71.1 | 317 | 108 | 241 | 188 |
| Ta (ppm) | 1 | 0.5 | 1.1 | 2.2 | 0.6 | 0.7 |
| Tb (ppm) | 0.95 | 1.04 | 0.62 | 1.69 | 0.76 | 0.76 |
| Th (ppm) | 18.15 | 21.5 | 5.72 | 76.2 | 12.15 | 14.15 |
| Tm (ppm) | 0.44 | 0.27 | 0.39 | 0.64 | 0.43 | 0.44 |
| U (ppm) | 3.45 | 2.6 | 3.35 | 4.31 | 1.57 | 1.8 |
| V (ppm) | 129 | 12 | 38 | 43 | 103 | 22 |
| W (ppm) | 1.7 | 1.1 | 0.9 | 1.1 | <0.5 | 0.5 |
| Y (ppm) | 29.7 | 23.8 | 23.6 | 46 | 26.8 | 28 |
| Yb (ppm) | 3.23 | 1.59 | 2.96 | 3.72 | 2.63 | 2.89 |
| Zr (ppm) | 294 | 343 | 389 | 699 | 295 | 260 |

Table A3.2: Geochemical analyses of samples from the Avawatz Mountains.

## REFERENCES CITED

Andrew, J.E., Walker, J.D., and Monastero, F.C., 2014, Evolution of the central Garlock fault zone, California: A major sinistral fault embedded in a dextral plate margin: Geological Society of America Bulletin, v. 127, p. 227–249, doi:10.1130/B31027.1.

Bidgoli, T.S., Amir, E., Walker, J.D., Stockli, D.F., Andrew, J.E., and Caskey, S.J., 2015, Low-temperature thermochronology of the Black and Panamint mountains, Death Valley, California: Implications for geodynamic controls on Cenozoic intraplate strain: Lithosphere, v. 7, p. 473–480, doi:10.1130/L406.1.

Blythe, A.E., and Longinotti, N., 2013, Exhumation of the southern Sierra Nevada–eastern Tehachapi Mountains constrained by low-temperature thermochronology: Implications for the initiation of the Garlock fault: Lithosphere, v. 5, p. 321–327, doi:10.1130/L252.1.

Brady III, R.H., 1986. Cenozoic Geology of the Northern Avawatz Mountains in Relation to the Intersection of the Garlock and Death Valley fault zones, San Bernardino County, California, University of California, Davis, Davis, California, Ph.D. thesis, 291 p.

Burbank, D.W., and Whistler, D.P., 1987, Temporally constrained tectonic rotations derived from magnetostratigiraphic data: Implications for the initiation of the Garlock fault, California: Geology, v. 15, p. 1172, doi:10.1130/0091-7613(1987)15<1172:TCTRDF>2.0.CO;2.

Burchfiel, B.C., and Stewart, J.H., 1966, “Pull-Apart” Origin of the Central Segment of Death Valley, California: Geological Society of America Bulletin, v. 77, p. 439, doi:10.1130/0016-7606(1966)77[439:POOTCS]2.0.CO;2.

Chinn, L.D. Low-Temperature Thermochronometry of the Avawatz Mountains; Implications for the Eastern Terminus and Inception of the Garlock Fault Zone: University of Washington Master’s Thesis, p. 48.

Davis, G.A., and Burchfiel, B.C., 1973, Garlock Fault: An Intracontinental Transform Structure, Southern California: Geological Society of America Bulletin, v. 84, p. 1407, doi:10.1130/0016-7606(1973)84<1407:GFAITS>2.0.CO;2.

Dixon, T.H., Miller, M., Farina, F., Wang, H., and Johnson, D., 2000, Present-day motion of the Sierra Nevada block and some tectonic implications for the

Basin and Range province, North American Cordillera: Tectonics, v. 19, p. 1–24, doi:10.1029/1998TC001088.

Dixon, T.H., and Xie, S., 2018, A kinematic model for the evolution of the Eastern California Shear Zone and Garlock Fault, Mojave Desert, California: Earth and Planetary Science Letters, v. 494, p. 60–68.

Dokka, R.K., and Travis, C.J., 1990, Role of the Eastern California Shear Zone in accommodating Pacific-North American Plate motion: Geophysical Research Letters, v. 17, p. 1323–1326.

Everden, J.F., Savage, D. E., Curtis, G. H., and James, G. T., 1964, Potassium-Argon dates and the Cenozoic mammalian chronology of North America: American Journal of Science, V. 262, P. 145-198.

Farley, K.A., 2000, Helium diffusion from apatite: General behavior as illustrated by Durango fluorapatite: Journal of Geophysical Research: Solid Earth, v. 105, p. 2903–2914, doi:10.1029/1999JB900348.

Flowers, R.M., Zeitler, P.K., Danišík, M., Reiners, P.W., Gautheron, C., Ketcham, R.A., Metcalf, J.R., Stockli, D.F., Enkelmann, E., and Brown, R.W., 2022, (U-Th)/He chronology: Part 1. Data, uncertainty, and reporting: Geological Society of America Bulletin special volume on the Reporting and Interpretation of Geochronologic data, https://doi.org/10.1130/B36266.1

Garfunkel, Z., 1974, Model for the Late Cenozoic Tectonic History of the Mojave Desert, California, and for Its Relation to Adjacent Regions: Geological Society of America Bulletin, v. 85, p. 1931, doi:10.1130/0016-7606(1974)85<1931:MFTLCT>2.0.CO;2.

Giorgis, S., Weber, J., Sanguinito, S., Beno, C., and Metcalf, J., 2017, Thermochronology constraints on Miocene exhumation in the Central Range Mountains, Trinidad: Geological Society of America Bulletin, v. 129, p. 171–178, doi:10.1130/B31363.1.

Guest, B., Pavlis, T. L., Golding, H., & Serpa, L. (2003). Chasing the Garlock: A study of tectonic response to vertical axis rotation. Geology, 31(6), 553–556. https://doi.org/10.1130/0091-7613(2003)031<0553

Guenthner, W., Reiners, P., Ketcham, R., Nasdala, L., Giester, G., 2013. Helium diffusion in natural zircon: radiation damage, anisotropy, and the interpretation of zircon (U-TH)/He thermochronology. American Journal of Science 313, 145–198.

Hamilton, W., and Myers, W.B., 1966, Cenozoic tectonics of the western United States: Reviews of Geophysics, v. 4, p. 509–549, doi:10.1029/RG004i004p00509.

Hatem, A.E., and Dolan, J.F., 2018, A Model for the Initiation, Evolution, and Controls on Seismic Behavior of the Garlock Fault, California: Geochemistry, Geophysics, Geosystems, v. 19, p. 2166–2178, doi:10.1029/2017GC007349.

Heaman, L.M., and Grotzinger, J.P., 1992, 1.08 Ga diabase sills in the Pahrump Group, California: Implications for development of the Cordilleran miogeocline: Geology, v. 20, p. 637–640, doi:10.1130/0091-7613(1992)020<0637:GDSITP>2.3.CO;2.

Henshaw, P.C. 1939, A Tertiary mammalian fauna from the Avawatz Mountains, San Bernardino County, California: Carnegie Institute, Washington Publication 5A, 30 p.

Hess, F.L., 1910, Gold mining in the Randsburg quadrangle, California: United States Geological Survey Bulletin 430, p. 23-47.

Hill, M.L., and Dibblee, T.W., 1953, SAN ANDREAS, GARLOCK, AND BIG PINE FAULTS, CALIFORNIA: Geological Society of America Bulletin, v. 64, p. 443, doi:10.1130/0016-7606(1953)64[443:SAGABP]2.0.CO;2.

Humphreys, E.D., and Weldon II, R.J., 1994, Deformation across the western United States: A local estimate of Pacific-North America transform deformation: Journal of Geophysical Research: Solid Earth, v. 99, p. 19975–20010, doi:10.1029/94JB00899.

Holm, D.K. and Dokka, R.K., 1991, Major Late Miocene cooling of the middle crust associated with extensional orogenesis in the Funeral Mountains, California. Geophysical Research Letters 18: doi: 10.1029/91GL02079

Holm, D.K., and Dokka, R.K., 1993, Interpretation and tectonic implications of cooling histories: An example from the Black Mountains, Death Valley extended terrane, California: Earth and Planetary Science Letters, v. 116, p. 63–80, doi:10.1016/0012-821X(93)90045-B.

Jahns, R.H., Troxel, B.W., and Wright, L.A., 1971, Some structural implications of a late Precambrian-Cambrian section in the Avawatz Mountains, California: Geological Society of America Abstracts with Programs, v. 3, p. 140.

Jahns, R.H, and Wright, L.A., 1960, The Garlock and Death Valley fault zones in the Avawatz Mountains, California (abs): Geological Society of America Bulletin, v. 71, p. 2063.

Jackson, S.E., Pearson, N.J., Griffin, W.L., Belousova, E.A., 2004, The application of laser ablation-inductively coupled plasma-mass spectrometry to in situ U-Pb zircon geochronology: Chemical Geology, v. 211, p. 47-69.

Ketcham, R., 2005, Forward and Inverse Modeling of Low-Temperature Thermochronometry Data, in Reviews in Mineralogy & Geochemistry, v. 58, p. 275–314, doi:10.2138/rmg.2005.58.11.

Lanphere, M.A., and Baadsgaard, H., 2001, Precise K-Ar, 40Ar/39Ar, Rb-Sr, and U-Pb mineral ages from the 27.5 Ma Fish Canyon Tuff reference standard: Chemical Geology, v. 175, p. 653-671.

Lee, J., Stockli, D.F., Owen, L.A., Finkel, R.C., and Kislitsyn, R., 2009, Exhumation of the Inyo Mountains, California: Implications for the timing of extension along the western boundary of the Basin and Range Province and distribution of dextral fault slip rates across the eastern California shear zone: Tectonics, v. 28, doi:10.1029/2008TC002295.

Lee, J., Stockli, D.F., and Blythe, A.E., 2023, Cenozoic slip along the southern Sierra Nevada normal fault, California (USA): A long-lived stable western boundary of the Basin and Range: Geosphere, v. 19, p. 1–22, https://doi.org/10.1130/GES02574.1.

Lima, R.D., Prior, M.G., Stockli, D.F., and Hayman, N.W., 2018, Protracted heating of the orogenic crust in Death Valley, California, USA: Geology, v. 46, p. 315–318, doi:10.1130/G39865.1.

McGill, S.F., and Sieh, K., 1991, Surficial offsets on the Central and Eastern Garlock Fault associated with prehistoric earthquakes: Journal of Geophysical Research: Solid Earth, v. 96, p. 21597–21621, doi:10.1029/91JB02030.

McGill, S.F., Wells, S.G., Fortner, S.K., Kuzma, H.A., and McGill, J.D., 2009, Slip rate of the western Garlock fault, at Clark Wash, near Lone Tree Canyon, Mojave Desert, California: Geological Society of America Bulletin, v. 121, p. 536–554, doi:10.1130/B26123.1.

Michael, E.D., 1966. Large lateral displacement on Garlock fault, California, as measured from offset fault system. Geological Society of America Bulletin, 77(1), pp.111-114.

Miller, M.M., Johnson, D.J., Dixon, T.H., and Dokka, R.K., 2001, Refined kinematics of the eastern California shear zone from GPS observations, 1993–1998: Journal of Geophysical Research: Solid Earth, v. 106, p. 2245–2263, doi:10.1029/2000JB900328.

Oskin, M., Perg, L., Shelef, E., Strane, M., Gurney, E., Singer, B., and Zhang, X., 2008, Elevated shear zone loading rate during an earthquake cluster in eastern California: Geology, v. 36, p. 507–510, doi:10.1130/G24814A.1.

Paton, C., Woodhead, J.D., Hellstrom, J.C., Hergt, J.M., Greig, A., Maas, R., 2010. Improved laser ablation U-Pb zircon geochronology through robust downhole fractionation correction. Geochemistry, Geophysics, Geosystems 11.

Paton, C., Hellstrom, J., Paul, B., Woodhead, J., Hergt, J., 2011, Iolite: Freeware for the visualization and processing of mass spectrometric data. Journal of Analytical Atomic Spectrometry, 26 (12), 2508-2518.

Petrus, J.A., Kamber, B.S., 2012. VizualAge: A Novel Approach to Laser Ablation ICP-MS U-Pb Geochronology Data Reduction. Geostandards and Geoanalytical Research 36, 247–270.

Pavlis, T.L., and Trullenque, G., 2021, Evidence for 40–41 km of dextral slip on the southern Death Valley fault: Implications for the Eastern California shear zone and extensional tectonics: Geology, v. 49, p. 767–772, doi:10.1130/G48528.1.

Platt, J.P., and Becker, T.W., 2013, Kinematics of rotating panels of E–W faults in the San Andreas system: what can we tell from geodesy? Geophysical Journal International, v. 194, p. 1295–1301, doi:10.1093/gji/ggt189.

Reiners, P., Brandon, M., 2006, Using Thermochronology to Understand Orogenic Erosion, Annual Review of Earth and Planetary Science, v. 34, p. 419-66

Reinert, E., 2004, Low-temperature thermochronometry of the Avawatz Mountains, California: Implications for the inception of the Eastern California Shear Zone, University of Washington Master's Thesis, 31 p.

Rittase, W.M., Kirby, E., McDonald, E., Walker, J.D., Gosse, J., Spencer, J.Q.G., and Herrs, A.J., 2014, Temporal variations in Holocene slip rate along the central Garlock fault, Pilot Knob Valley, California: Lithosphere, v. 6, p. 48–58, doi:10.1130/L286.1.

Sample, B., 2018, Provenance of Miocene Strata of the El Paso Basin, Southern California: Constraints on the Late Cenozoic Paleogeography of the Southern Sierra Nevada Region.

Sanderson, D.J., and Marchini, W.R.D., 1984, Transpression; Journal of Strucutral Geology, v. 6(5), p. 449-458.

Schermer, E.R., Luyendyk, B.P., and Cisowski, S., 1996, Late Cenozoic structure and tectonics of the northern Mojave Desert: Tectonics, v. 15, p. 905–932, doi:10.1029/96TC00131.

Sizemore, T., Wielicki, M.M., Çemen, I., Stockli, D., Heizler, M., and Robinson, D., 2019, Structural evolution of central Death Valley, California, using new thermochronometry of the Badwater turtleback: Lithosphere, v. 11, p. 436–447, doi:10.1130/L1044.1.

Smith, G., 1962, Large lateral displacement on Garlock fault, California, as measured from offset dike swarm: American Association of Petroleum Geologists Bulletin, v. 46, p. 85–104.

Stewart, J.H., 1983, Extensional tectonics in the Death Valley area, California: Transport of the Panamint Range structural block 80 km northwestward: Geology, v. 11, p. 153.

Spencer, J., 1981, Geology and Geochronology of the Avawatz Mountains, San Bernardino County, California, Massachusetts Institute of Technology, Cambridge, Massachusetts, Ph.D. thesis, 183 p.

Spencer, J.E., 1990, Geologic Map of the Southern Avawatz Mountains, Northeastern Mojave Desert Region, San Bernardino County, California. U.S. Geological Survey. Miscellaneous Field Studies Map MF-2117.

Stuart, W. D. (1991). Cause of the Garlock fault. Geological Society of America, 23(5), 198.

Thatcher, W., Savage, J.C., and Simpson, R.W., 2016, The Eastern California Shear Zone as the northward extension of the southern San Andreas Fault: Journal of Geophysical Research: Solid Earth, v. 121, p. 2904–2914, doi:10.1002/2015JB012678.

Troxel, B.W., Butler, P.R., 1979, Tertiary and Quaternary fault history of the intersection of the Garlock and Death Valley fault zones, southern Death Valley, California: unpublished report submitted to the U.S. Geological Survey, Menlo Park, California 29 p.

Troxel, B., Wright, L., Jahns, R., 1972, Evidence for differential displacement along the Garlock fault zone, California: Geological Society of America Abstracts with Programs, v. 5, p. 250.

Walker, J.D., Bidgoli, T.S., Diderickson, B.D., Stockli, D.F., and Andrew, J.E., 2014, Middle Miocene to recent exhumation of the Slate Range, eastern California, and implications for the timing of extension and the transition to transtension: Geosphere, v. 10, p. 276–291, doi:10.1130/GES00947.1.

Wright, L.A., and Troxel, B.W., 1967, Limitations on right-lateral strike-slip displacement, Death Valley and Furnace Creek fault zones, California: Geological Society of America Bulletin, v. 78, n. 8, p. 933-949.

Zheng, D., Zhang, P.Z., Wan, J., Yuan, D., Li, C., Yin, G., Zhang, G., Wang, Z., Min, W. and Chen, J., 2006, Rapid exhumation at~ 8 Ma on the Liupan Shan thrust fault from apatite fission-track thermochronology: Implications for growth of the northeastern Tibetan Plateau margin. Earth and Planetary Science Letters, 248(1-2), pp.198-208.

Zuza, A. V., Cheng, X., & Yin, A., 2016, Testing models of Tibetan Plateau formation with Cenozoic shortening estimates across the Qilian Shan–Nan Shan thrust belt. Geosphere, 12(2), 501-532.